AFRL-AFOSR-VA-TR-2019-0121

The Onset of Dynamic Stall: Understanding Flowfield Unsteadinessto Enable Closed-Loop Control

Phillip Ansell
UNIVERSITY OF ILLINOIS

04/19/2019
Final Report

Air Force Research Laboratory
AF Office Of Scientific Research (AFOSR)/ RTA1
Arlington, Virginia 22203
Air Force Materiel Command

REPORT DOCUMENTATION PAGE	*Form Approved* *OMB No. 0704-0188*

1. REPORT DATE *(DD-MM-YYYY)*
30-03-2019

2. REPORT TYPE
Final Report

3. DATES COVERED *(From - To)*
01-08-2015 - 31-12-2018

4. TITLE AND SUBTITLE
The Onset of Dynamic Stall: Understanding Flowfield Unsteadiness to Enable Closed-Loop Control

5a. CONTRACT NUMBER

5b. GRANT NUMBER
FA9550-15-1-0277

5c. PROGRAM ELEMENT NUMBER

6. AUTHOR(S)
Ansell, Phillip, J.

5d. PROJECT NUMBER

5e. TASK NUMBER

5f. WORK UNIT NUMBER

7. PERFORMING ORGANIZATION NAME(S) AND ADDRESS(ES)
The Board of Trustees of the University of Illinois
Henry Administration Building
506 S. Wright Street
Urbana, IL 61801

8. PERFORMING ORGANIZATION REPORT NUMBER

9. SPONSORING/MONITORING AGENCY NAME(S) AND ADDRESS(ES)
Air Force Office of Scientific Research
875 N. Randolph, Ste.325, Rm. 3112
Arlington VA 22203-1768

10. SPONSOR/MONITOR'S ACRONYM(S)
AFOSR/RTA-1

11. SPONSOR/MONITOR'S REPORT NUMBER(S)

12. DISTRIBUTION/AVAILABILITY STATEMENT
Distribution A

13. SUPPLEMENTARY NOTES

14. ABSTRACT

The current study was conducted in order to characterize the quantitative spatiotemporal scales associated with the dynamic stall flow field across a transitional-Reynolds number regime. Across these higher Reynolds numbers, a series of flow field interactions were observed to produce a broad distribution of scales not observed in the canonical dynamic stall process at lower Reynolds numbers from the literature.

From this study, unsteady flow oscillations associated with a laminar separation bubble were identified. These oscillations emerged prior to the inception of the dynamic stall process, and were observed to follow a Strouhal number scaling of 1.2, when the separation bubble height was used as the characteristic length scale. Further study of the off-body velocity field revealed variations in the developmental morphology of the dynamic stall vortex with changing Reynolds number. An Empirical Mode Decomposition method was coupled to a Hilbert spectral analysis method to provide a quantitative characterization of the temporal scales that emerge during unsteady separation and dynamic stall vortex formation.

15. SUBJECT TERMS
Dynamic stall, unsteady aerodynamics, empirical mode decomposition, Hilbert-Huang transform, time-frequency analysis

16. SECURITY CLASSIFICATION OF:			17. LIMITATION OF ABSTRACT	18. NUMBER OF PAGES	19a. NAME OF RESPONSIBLE PERSON
a. REPORT	b. ABSTRACT	c. THIS PAGE			Phillip J. Ansell
U	U	U	UU		19b. TELEPHONE NUMBER *(Include area code)* (217) 300-0949

Reset

The Onset of Dynamic Stall: Understanding Flowfield Unsteadiness to Enable Closed-Loop Control

Agreement # FA9550-15-1-0277

Final Report

Principal Investigator:
Phillip J. Ansell
Department of Aerospace Engineering
University of Illinois at Urbana-Champaign
306 Talbot Laboratory, MC-236
104 South Wright Street
Urbana, Illinois 61801
ansell1@illinois.edu
(217) 300-0949

Overview

The enclosed Final Report documents the significant findings produced at the conclusion of the research program. An overview of objectives, relevant findings, and information regarding personnel and dissemination of results are provided.

Objectives

The objectives of the study included:

- Characterize the spatio-temporal spectral content of unsteady C_p during dynamic stall
- Understand time-frequency scaling of unsteady shear-layer vorticity buildup prior to dynamic stall onset
- Relate oscillations in surface pressure measurements to the onset of dynamic stall in the airfoil flow field through a reduced-order model

The originally-proposed task timeline for the current study is provided in Fig. 1. At the conclusion of the research program, all scientific goals were completed, with no delays to the original programmatic scheduling.

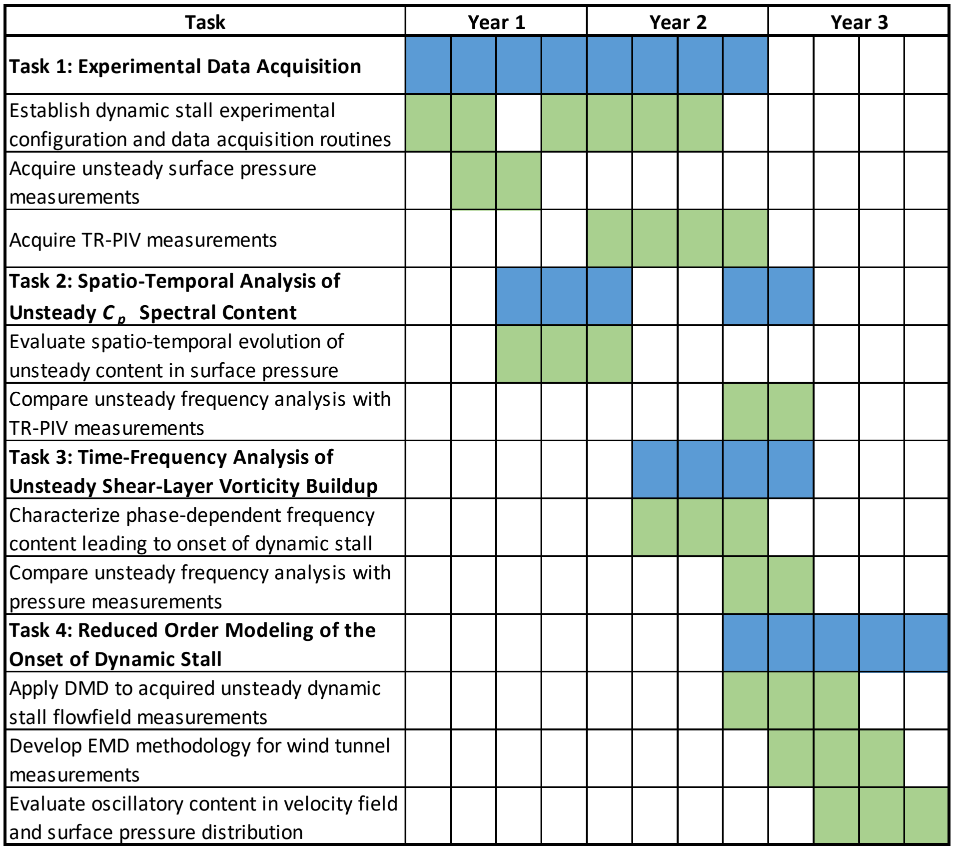

Task	Year 1				Year 2				Year 3			
Task 1: Experimental Data Acquisition	🟦	🟦	🟦	🟦	🟦	🟦	🟦	🟦				
Establish dynamic stall experimental configuration and data acquisition routines	🟩	🟩		🟩	🟩	🟩	🟩					
Acquire unsteady surface pressure measurements		🟩	🟩									
Acquire TR-PIV measurements					🟩	🟩	🟩	🟩				
Task 2: Spatio-Temporal Analysis of Unsteady C_p Spectral Content			🟦	🟦	🟦			🟦	🟦			
Evaluate spatio-temporal evolution of unsteady content in surface pressure			🟩	🟩	🟩							
Compare unsteady frequency analysis with TR-PIV measurements								🟩	🟩			
Task 3: Time-Frequency Analysis of Unsteady Shear-Layer Vorticity Buildup						🟦	🟦	🟦	🟦			
Characterize phase-dependent frequency content leading to onset of dynamic stall						🟩	🟩	🟩				
Compare unsteady frequency analysis with pressure measurements								🟩	🟩			
Task 4: Reduced Order Modeling of the Onset of Dynamic Stall								🟦	🟦	🟦	🟦	🟦
Apply DMD to acquired unsteady dynamic stall flowfield measurements								🟩	🟩	🟩		
Develop EMD methodology for wind tunnel measurements									🟩	🟩	🟩	
Evaluate oscillatory content in velocity field and surface pressure distribution										🟩	🟩	🟩

Fig. 1 Proposed task timeline for study.

Introduction

Dynamic stall is a complex phenomenon in aerodynamics, which occurs for wings and bodies subject to unsteady separation due to rapid changes in relative freestream conditions. The onset of dynamic stall is associated with drastic increases in flow field unsteadiness, producing high levels of airframe vibratory loading as well as an overall impairment of vehicle aerodynamic performance. While it is most commonly regarded as a hazard for rotorcraft in forward flight, dynamic stall can also occur for fixed wing aircraft under severe gust loading and during rapid or extreme maneuvers. Additionally, dynamic stall occurs during the rapid pitch-up associated with perching maneuvers, which then progresses into a post-stall flow field.[1,2] The transient and highly unsteady nature of these types of flow fields make them substantially difficult to predict and simulate.

Traditionally dynamic stall has been studied using airfoils undergoing unsteady motions, like pitching, plunging, or a combination pitch/plunge. Several seminal investigations [3–10] have led to an improved understanding of the general features of dynamic stall on oscillating airfoils, including the influence of the dynamic stall vortex (DSV), the presence of hysteresis and pitch damping, and the classification of light and deep dynamic stall regimes. A summary of the dynamic stall process, and its effects on the airfoil normal force and pitching moment coefficients, is presented in Fig. 2, after Carr.[4]

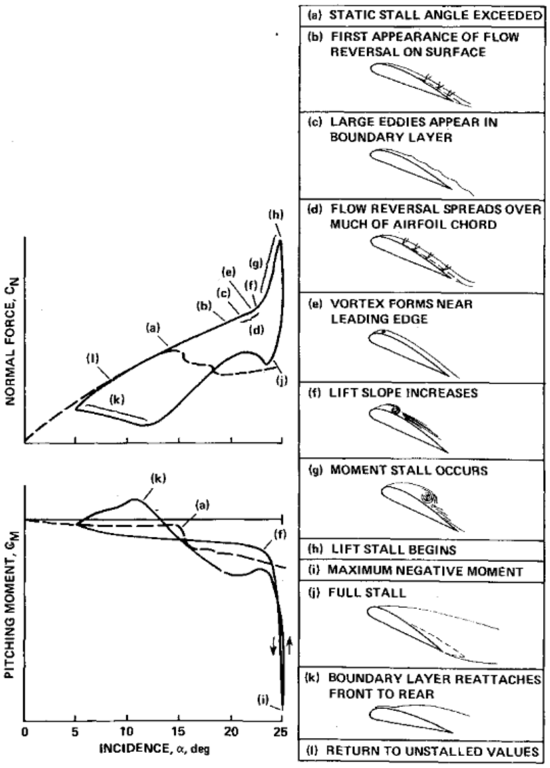

Fig. 2 Summary of dynamic stall process, after Carr[4]; dashed lines in C_n and C_m polars indicate static airfoil values.

From Fig. 2, during dynamic stall the lift coefficient of an airfoil exceeds the maximum lift coefficient of the static airfoil. A DSV emerges from the airfoil leading-edge region, which acts to augment the airfoil lift. The emergence of this DSV is conventionally used to designate the instance of the "onset" of dynamic stall. As the angle of attack of the airfoil is further increased during the dynamic maneuver, the DSV is moved downstream, producing large levels of suction near the airfoil trailing edge, which contribute to a strong nose-down pitching moment. With subsequent increases in angle of attack, this DSV moves away from the airfoil surface, leading to significant reduction in lift coefficient and flow separation across the entire upper surface of the airfoil. Due to hysteresis effects, the airfoil angle of attack must be reduced below the static stall angle of attack in order for an attached boundary layer to be re-established.

Recent work has provided a preliminary understanding of the unsteady dynamic stall flow field by means of phase-averaged and time-resolved particle image velocimetry, as well as high-fidelity simulations. Pruski and Bowersox [11] performed phase-averaged particle image velocimetry experiments on a dynamically pitching airfoil and compared the instantaneous and phase-averaged characteristics of the DSV flow field. These authors identified that in an instantaneous sense the DSV is formed through a collective amalgamation of multiple vortical structures. The authors also documented the phase-dependent magnitude of velocity fluctuations near the airfoil leading edge using a Hilbert transform technique. Mulleners and Raffel [12,13] performed time-resolved particle image velocimetry experiments to study the development of dynamic stall on a sinusoidally oscillating airfoil. The dynamic stall process was classified into a primary instability stage, characterized by the development of small-scale instabilities in the shear layer, and vortex development stage, characterized by non-linear interactions that lead to the roll up of the shear layer that eventually lead to the formation of the DSV. Furthermore, the process of DSV separation was identified as being very similar to a canonical vortex-induced separation process. Large-eddy simulation results of Visbal [14] provided detailed insights into the unsteady behavior of the boundary layer over an airfoil during dynamic stall, along with the temporal evolution of a leading-edge laminar separation bubble (LSB) and the inception and growth of the DSV. Most notably, in this study the highest extent of unsteadiness in the flow field of the pitching airfoil was identified prior to the emergence of the DSV. This observation was consistent with the findings of Lorber and Carta [15], where a distinct increase in $C_{p,rms}$ was observed near the airfoil leading-edge region prior to the emergence of the DSV.

The objectives of the current study are to understand the influence of transitional Reynolds numbers on the evolution of the boundary layer, with particular emphasis on the LSB and a characterization of the instantaneous frequency scales in the flow associated with the dynamic stall development. Additionally, a significant goal of the current study is to capture the unsteady separation flow morphology at transitional Reynolds numbers across the airfoil upper surface, particularly during the emergence of the DSV.

Experimental Methods

Experimental Environment

All of the experiments were conducted at the University of Illinois in a 2.8-ft × 4-ft open-return type, low speed, low turbulence (Tu < 0.1%) wind tunnel, shown in Fig. 3. An NACA 0012 airfoil model with a chord length (*c*) of 1.5 ft. was used for the present study. This model was installed vertically inside the test section and spanned the entire height of the test section. The NACA 0012 airfoil section was selected since it has been used extensively in the past for dynamic stall investigations. The airfoil model was constructed in three different sections, as shown in Fig. 4 a). The center-span section of the model was manufactured from aluminum with a hollow interior, and it extended 6 inches in the spanwise direction. The exterior sections were manufactured with a foam core and a fiberglass skin, which was done in an effort to reduce the inertia of the model. The experiments in this study were performed at three different chord-based Reynolds numbers, $Re_c = 0.2 \times 10^6$ ($M_\infty = 0.02$), 0.5×10^6 ($M_\infty = 0.05$), and 1×10^6 ($M_\infty = 0.1$), which were controlled to within 1% during testing. Only off-body velocity field data were acquired for the case of $Re_c = 0.2 \times 10$, as the pressure transducer systems utilized in this study were not suited for the low-pressure values produced across the airfoil surface.

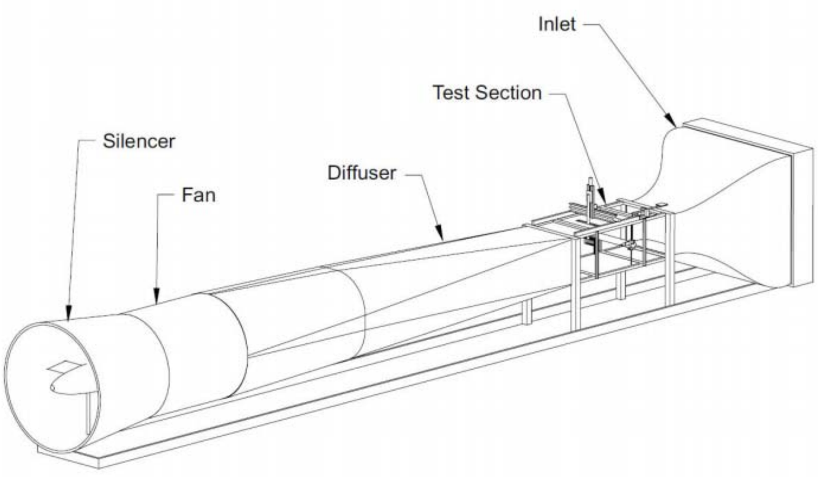

Fig. 3 Schematic of the University of Illinois 2.8-ft × 4-ft wind tunnel.

The model was subjected to a dynamic pitch maneuver along a linear ramp using a high-speed, high-torque direct drive brushless servo motor, model C(H)092 manufactured by Kollmorgen Corporation. The servo motor was driven by an AKD servo drive with closed-loop feedback control provided by an NI PCI-7354 motion controller. A computer rendering of the dynamic stall setup is shown in Fig. 4 c). A linear ramp motion profile with a prescribed dimensionless pitch rate, defined by Eq. 1, was chosen in order to isolate the dynamic stall process from boundary-layer hysteresis and the unsteady wake effects of periodic maneuvers.

$$\omega^+ = \frac{\omega c}{U_\infty} \tag{1}$$

A pitch rate of $\omega^+ = 0.05$ was used during the current study, since it has been studied in the past using high-fidelity simulations. The angular position of the airfoil was also monitored in real time using a high-resolution Dynapar HS35R optical encoder, which was attached directly to the airfoil rotary shaft. The unsteady surface pressure measurements in this study were acquired between -5 deg $\leq \alpha \leq$ 30 deg. The motor was, however, configured to rotate between -6 deg $\leq \alpha \leq$ 31 deg in order to reduce the effects of acceleration from the intended linear pitch profile between -5 deg $\leq \alpha \leq$ 30 deg. An example of the motion profile produced for the airfoil at $Re_c = 0.5 \times 10^6$ and for a pitch rate of $\omega^+ = 0.05$ is shown in Fig. 5.

Surface Pressure Acquisition and Processing

The center section of the airfoil model was fitted with 27 ultra-miniature, high-frequency response unsteady pressure transducers. These transducers were manufactured by Kulite Semiconductor Products, Inc. under model designation XCS-062 and had a differential pressure range of ±5 psi. The distribution of these pressure transducers across the model surface is shown in Fig. 4 b). The unsteady pressure signals from all of the transducers were acquired using a National Instruments Signal Conditioning eXtensions for Instrumentation (SCXI) measurement system. These signals were acquired at two different sampling frequencies, f_{acq} = 3 kHz and 33 kHz respectively.

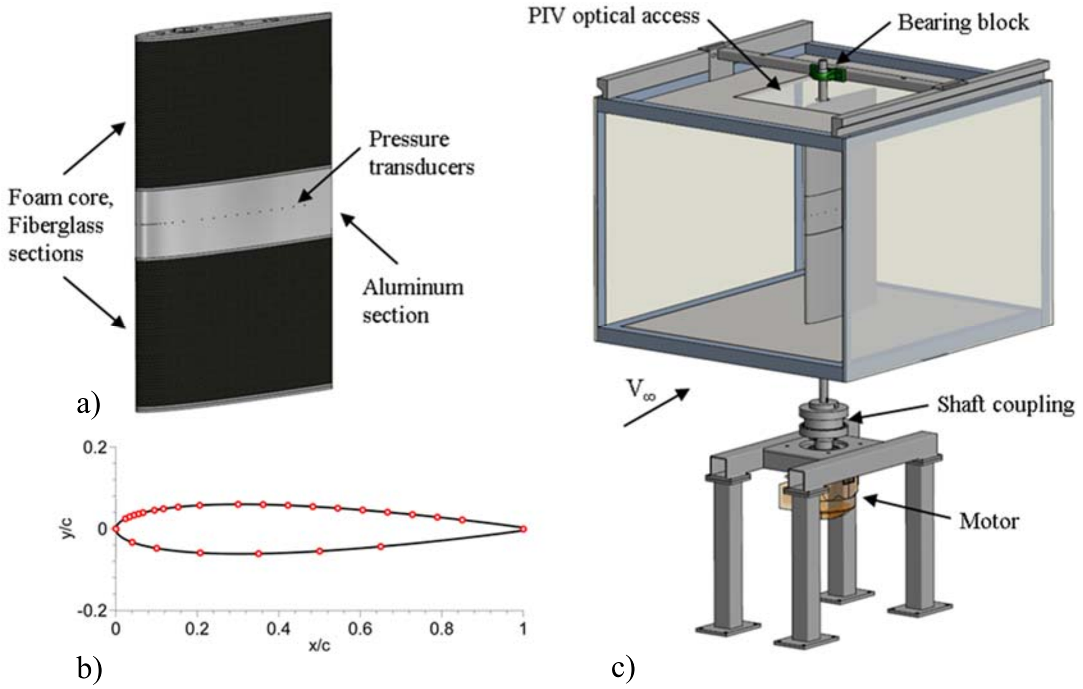

Fig. 4 a) CAD model of the NACA 0012 airfoil featuring a three-section construction, b) distribution of unsteady pressure transducers across the airfoil surface, and c) a computer rendering of the Dynamic Stall setup with all the major components.

The simultaneous sampling capability of the SCXI system was employed for measurements acquired at f_{acq} = 3 kHz in order to eliminate phase differences and to ensure temporal coherence between C_p datasets acquired across multiple chordwise locations over the surface of the airfoil. The instantaneous pressure distribution acquired at the low sampling frequency was also used to determine the time-dependent lift and quarter-chord pitching moment coefficients (C_l and C_m, respectively) of the airfoil. Due to hardware sampling limitations, however, the high frequency measurements at f_{acq} = 33 kHz were acquired individually across select chordwise stations on the airfoil upper surface. The SCXI system was also configured with a low-pass Bessel filter set to the Nyquist frequency for each sampling rate to prevent signal aliasing. The acquired wind tunnel data were corrected to compensate for solid blockage and streamline curvature effects through standard tunnel correction procedures following the standard methods discussed by Barlow et al.[16]

The time-dependent spectral content of unsteady C_p was obtained from the high frequency C_p measurements by performing a continuous wavelet transform (CWT) of the acquired pressure signal using a Morlet wavelet. The Morlet wavelet was used in this study since it has a complex-valued wavelet function, which is extremely effective in the identification of oscillatory behaviors in a signal [17]. Furthermore, the Morlet wavelet scale is approximately equivalent to the corresponding Fourier scale. Therefore, the spectral measurements in this study were translated conveniently from the wavelet transform frequency scales to the corresponding Fourier transform frequencies.

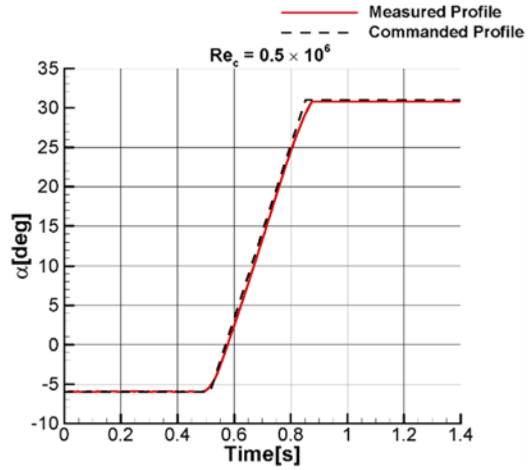

Fig. 5 Example airfoil motion profile acquired during dynamic pitch at $Re_c = 0.5 \times 10^6$ for an $\omega^+ = 0.05$ linear ramp maneuver; the commanded motion profiles sent to the motor is also included for reference.

Off-Body Velocity Field Acquisition and Processing

Time-resolved particle image velocimetry (TR-PIV) data were also acquired during a dynamic pitch for an angle-of-attack range of 5 deg $\leq \alpha \leq$ 30 deg. These data were acquired across a horizontal plane near the mid-span of the airfoil model. A 60 W Quantronix Darwin Duo Nd: YLF laser was used, in conjunction with a series of beamforming optics, to produce a laser sheet spread across the entirety of the airfoil chord. The laser was operated in external double trigger mode to provide a pair of laser pulses at a repetition rate of 1 kHz. A mineral oil based haze generator was used to seed the flow. The airfoil was wrapped in black contact paper to reduce the intensity of reflections off the surface of the model. The images of tracer particles were acquired at 2 × 10^3 fps using a Photron Mini AX200 CMOS high-speed camera at a resolution of 1024 × 1024 pixel, which also corresponds to the maximum resolution of the camera. The high-speed camera was equipped with a photographic lens set at a focal length, $f = 28$mm and at an f-number setting of $f_{\#} = 2.8$. The laser and camera system were configured in frame-straddling mode, resulting in a velocity field acquisition frequency of 1 kHz. The acquired PIV images were processed in LaVision DaVis version 8.4.0 using multi-pass cross correlation techniques with an adaptive interrogation window. The interrogation window size in the initial step was set at 128 × 128 pixels at 50% overlap, which was decreased down to 16 × 16 pixels at 75% overlap in the final processing step.

One of the significant goals of the current study was to identify the quantitative scales in the off-body velocity field through the use of modal decomposition. However, identifying well-defined modal contributions of the dynamic stall flow development poses a significant challenge for two notable reasons. First, the unsteady separation and vortex roll-up process represents a dynamic nonlinear system that is generally not well represented by a simple linearization about a steady-state solution. Second, dynamic stall is an inherently transient process, where the flow variables are not characterized by a well-defined mean, but rather a time-dependent trend. These factors significantly limit the modal decomposition approaches that can be applied, particularly when projecting onto a single linear basis composed of fixed spatial or Fourier modes across the entire dynamic stall process. For example, during the unsteady separation process associated with a dynamically pitching airfoil, the characteristic spatial and temporal scales of the flow are expected to change with the airfoil incidence. A low-order representation based on a small set of modes that represent fixed length or time scales across the entire oscillation cycle will not be able to fully describe the dynamically-evolving flow in the case of dynamic stall. Large-scale features that are statistically dominant, such as the large-scale dynamic stall vortex for sinusoidal variations in angle of attack, can be represented by dominant POD modes, however it is also desirable to utilize modal analysis to understand the small-scale flow structures that contribute to the development of this large-scale vortex structure.

For this reason, the empirical mode decomposition (EMD) signal processing method will be used in the current study, which is an adaptive, scale-based modal decomposition technique. The velocity fields were selected for this decomposition over other flow variables as they represent a directly-measured, physical quantity that embodies the multi-scale nature of the flow field. Other flow variables, such as the vorticity field, are less suitable for EMD analysis in the current study due to the lumped non-zero mean influence produced by individual vortical flow structures. In contrast, the velocity field produced by vortex-dominated flows is well-represented by IMFs, which are defined as purely oscillatory functions with zero mean. Additionally, the multi-scale vortical flow influences are best resolved when considering multiple velocity components, rather than the velocity magnitude field, requiring the inclusion of multivariate considerations during decomposition. Additionally, these vortical flow structures were resolved across a planar field (x,y) across the airfoil surface, as a function of time (t). As a result, maintaining modal dependence on all three dimensions was deemed important to properly observe the dynamical evolution of the flow field. In order to accomplish these requirements, the Fast and Adaptive Multidimensional, Multivariate Empirical Mode Decomposition (FA-MVEMD) method was used [18].

This decomposition approach provided a complete basis for the velocity field, such that the original velocity signal could be reproduced through a summation of all Intrinsic Mode Functions (IMFs) and the remaining residual (R).

$$\boldsymbol{V}(x,y,t) = \sum_{k=1}^{K} \boldsymbol{IMF}_k(x,y,t) + \boldsymbol{R}(x,y,t) \tag{2}$$

Since a multivariate EMD approach is used, the IMFs and residual are vector quantities of velocity, containing *x* and *y* components

$$\boldsymbol{IMF}_k(x,y,t) = u_k(x,y,t)\hat{\imath} + v_k(x,y,t)\hat{\jmath} \tag{3}$$

After computation of the resulting IMFs, a Hilbert spectral analysis was performed across the temporal domain locally at each position across the flow field. This approach allowed the time-dependent variation in the amplitude and phase angle of oscillatory content in the velocity field at each spatial point to be determined. The velocity scalar for each IMF was used in order to determine the Hilbert spectral content. The resulting representation of these oscillations can thus be expressed in the form,

$$V(t) = A(t)e^{i\theta(t)} \tag{4}$$

Taking the time derivative of the phase angle results in the recovery of the instantaneous angular frequency. Using this approach, the off-body temporal scales associated with each IMF were identified, along with their time-varying amplitude.

Results

Airfoil Performance

Measurements of the phase-averaged lift and quarter-chord pitching moment coefficients for the dynamically pitching NACA 0012 airfoil model at $Re_c = 0.5 \times 10^6$ are presented in Fig. 6 a) and b), respectively. These measurements are provided for both the clean airfoil model and for the model configured with a BL-trip, which was installed close to the airfoil leading edge. The performance of the clean airfoil, acquired under steady flow conditions, is also presented in Fig. 6 for comparison. Under steady conditions, the airfoil is observed, from Fig. 6 a), to attain a maximum lift coefficient of $C_{l,max} = 1.18$. The corresponding stall angle of attack is measured at

α_{stall} = 12.63 deg. The quarter-chord pitching moment coefficient of the airfoil, also under steady conditions, is observed, from Fig. 6 b), to be approximately equal to $C_m \approx 0$, for $\alpha < \alpha_{stall}$.

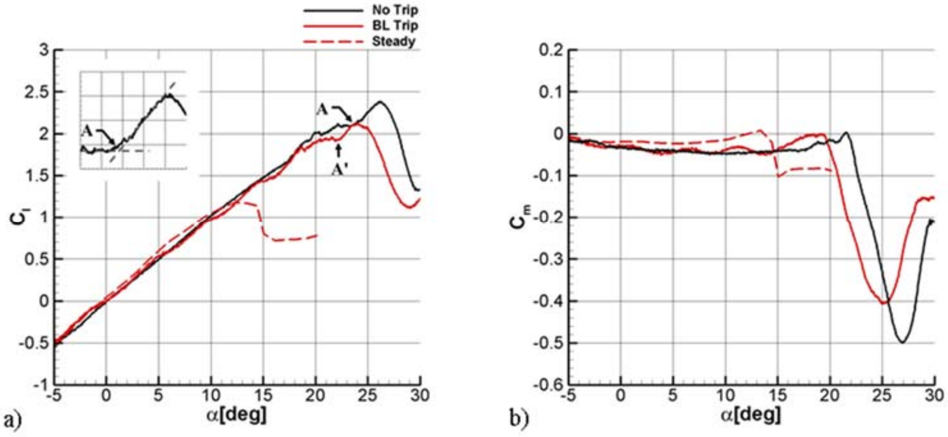

Fig. 6 Steady and unsteady a) C_l and b) C_m measurements for the NACA 0012 at $Re_c = 0.5 \times 10^6$.

In contrast with the steady measurements, the dynamic performance of the airfoil for both the clean and tripped configurations are associated with a large overshoot in the magnitude of lift and quarter-chord pitching moment coefficients and a significant delay in stall. A distinct increase in the lift curve slope can also be identified from the lift polars for both configurations prior to the occurrence of stall. This feature is indicated by arrows 'A' and 'A'' in Fig. 6 a). The increase in the lift curve slope is conjectured to result from a rapid spatial growth of the DSV, which causes increased suction across the upper surface of the airfoil. While the dynamic performances for both the clean and tripped airfoil configurations are observed to be qualitatively similar, there exists some notable quantitative differences. From Fig. 6 a), the maximum lift coefficient associated with the clean airfoil, $C_{l,max}$ = 2.37, is observed to be noticeably greater than the corresponding maximum attained by the tripped airfoil, measured at $C_{l,max}$ = 2.13. The lift stall angle of attack for the clean airfoil, indicated by arrow 'D' in Fig. 6 a), is identified at α_{stall} = 26.14 deg. This value of α_{stall} is also observed to be significantly greater than the corresponding measurement of α_{stall} = 23.92 deg, acquired for the tripped airfoil. Thus, the addition of the BL-trip promotes an early stall and produces a reduction in the maximum lift of the airfoil. A similar trend is observed for the quarter-chord pitching moment coefficient. The tripped airfoil $C_{m,min}$ = -0.4 is observed to be noticeably lower in magnitude as compared to $C_{m,min}$ = -0.5 observed for the clean airfoil. Furthermore, the angle of attack corresponding to $C_{m,min}$ for the tripped airfoil, α_{min} = 25.07 deg, indicated by arrows 'F' in Fig. 6b), is significantly lower than the corresponding α_{min} = 26.94 deg, measured for the clean airfoil.

Evolution of the Surface Pressure Field

A three-dimensional surface plot of the phase-averaged pressure field, $C_p(x,\alpha)$, acquired across the upper surface of the clean airfoil at $Re_c = 0.5 \times 10^6$, is presented in Fig. 7 a). For additional clarity, a projection of this C_p surface near the airfoil leading edge, between $0 \leq x/c \leq 0.3$, is also presented in Fig. 7 b) for 5 deg $\leq \alpha \leq$ 25 deg. Individual $C_p(x)$ distributions across the upper surface of the clean airfoil at select angles of attack are shown in Fig. 8. For α = 10.73 deg and 17.97 deg, corresponding to Fig. 8 b) and e), the tripped airfoil C_p distributions are also presented along with the C_p distributions corresponding to the clean airfoil, for the purposes of comparison. The location of the pressure transducers on the airfoil surface have also been indicated in Fig. 7 and Fig. 8. The discussion in relation to the behavior of unsteady separation will also be further supported by off-body velocity field data acquired by TR-PIV.

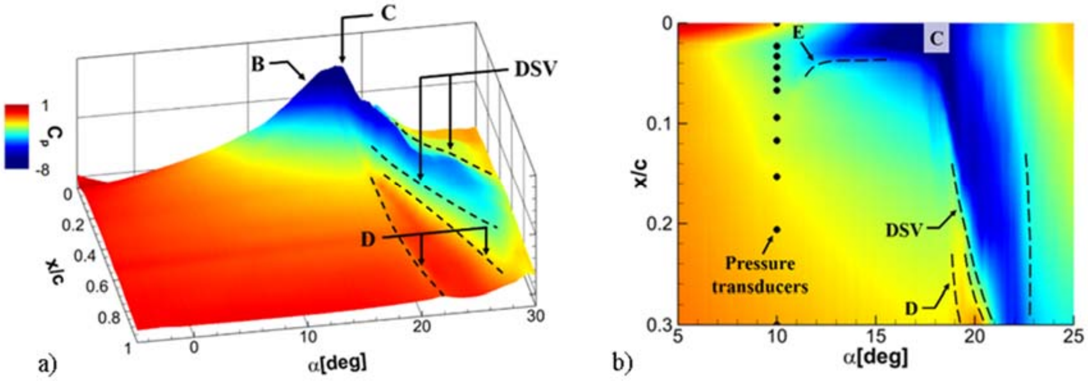

Fig. 7 Surface plots of the phase-averaged pressure measurements acquired a) across the entire upper surface of the airfoil and b) near the airfoil leading edge between $0 \leq x/c \leq 0.3$, at $Re_c = 0.5 \times 10^6$.

From Fig. 7, the initial phase of the dynamic stall process is characterized by a monotonic growth in suction near the leading edge of the airfoil. A sample C_p distribution acquired during the inviscid phase of the process is presented in Fig. 8 a). A characteristic plateau in the clean-airfoil C_p distribution begins to appear near the leading edge with further increase in the angle of attack. This feature can be identified in the C_p distribution at α = 10.73 deg, as indicated by arrow 'F' in Fig. 8 b). These pressure plateaus have been observed in literature to correspond to the formation of an LSB. The largely constant pressure region resulting from laminar separation of the flow near the airfoil leading edge is followed by rapid pressure recovery, due to turbulent reattachment, as indicated by arrow 'F'' in Fig. 8 b).

The laminar-turbulent bypass transition of the BL, in the presence of the BL trip, leads to increased near-wall momentum mixing which prevents flow separation from the airfoil surface. Thus, the pressure plateau feature, observed for the clean airfoil at α = 10.73 deg, is absent from the corresponding C_p distribution for the tripped BL, as indicated by arrow 'G' in Fig. 8 b). Moreover, the suction magnitude for the tripped airfoil configuration, without the LSB, is observed to be significantly greater than the magnitude of suction for the clean airfoil at the corresponding angle of attack. These observations provide further evidence for the presence of a laminar separation bubble, in the absence of forced transition, near the leading edge for the clean airfoil.

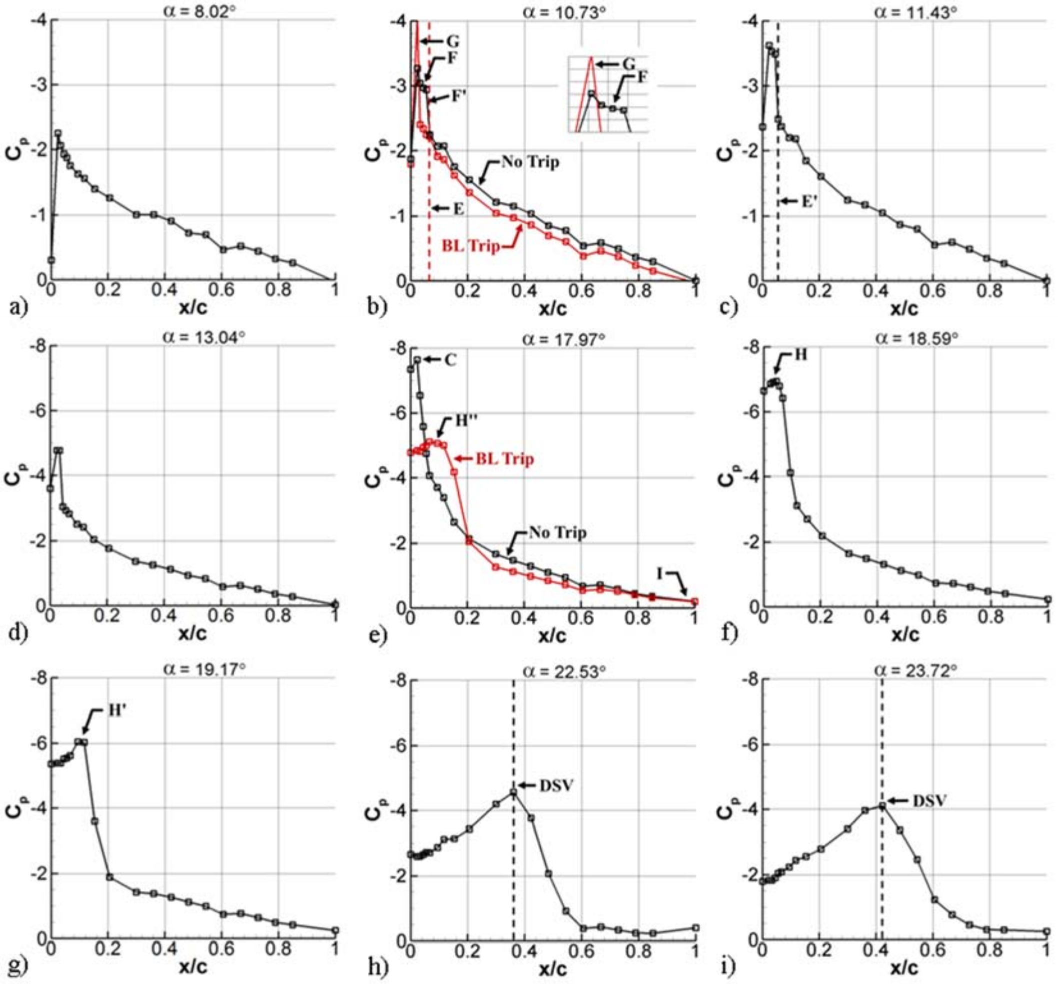

Fig. 8 Individual phase-averaged surface pressure measurements across the airfoil upper surface at a) α = 8.02 deg, b) α = 10.73 deg, c) α = 11.43 deg, d) α = 13.04 deg, e) α = 17.97 deg, f) α = 18.59 deg, g) α = 19.17 deg, h) α = 22.53 deg, and i) α = 23.72 deg, for $Re_c = 0.5 \times 10^6$.

The LSB reattachment point, estimated from literature as the edge of the sharp pressure recovery region, moves upstream with increasing angles of attack due to increasingly strong adverse pressure gradients. This movement of the reattachment point is indicated by arrows 'E' and 'E'' in Fig. 8 b) and c). The motion of LSB reattachment is also traced by a dashed curve, as indicated by arrow 'E' in Fig. 7 b). The spatial contraction of the LSB that is observed with increasing angle of attack is consistent with the observed behavior of separation bubbles in the literature across similar Reynolds number regimes. Further increase in the airfoil angle of attack causes the LSB to attain a minimum size, beyond which the location of the reattachment point on the airfoil surface remains largely independent of the angle of attack, as seen in Fig. 7 b). Increasing the angle of attack also produces a rapid growth in leading edge suction, as indicated by arrow 'B' in Fig. 7 a). This growth in suction can also be discerned by inspecting the relative magnitude of $C_{p,min}$ amongst the C_p distributions presented in Fig. 8 b), c) and d). The magnitude of suction eventually attains a global maximum, as indicated by arrow ‘C’ in Fig. 7 a) and Fig. 8 e).

During peak suction, the leading-edge pressure distribution reaches a value of $C_{p,min}$ = -7.40 at α = 17.97 deg. In addition to peak suction, the C_p distribution at α = 17.97 deg is also associated with reduced pressure recovery near the airfoil trailing edge, as indicated by arrow ‘I’ in Fig. 8 e). The incomplete pressure recovery is indicative of trailing-edge flow separation, which is conjectured to be distinct from the laminar separation event near the leading edge of the airfoil. Increments in the angle of attack beyond the maximum suction phase of the dynamic stall process is accompanied by a rapid decrease in suction near the airfoil leading edge, as indicated by arrow ‘H’ in Fig. 8 f). The collapse in suction has been demonstrated through computational simulations to result from LSB breakdown or ‘bursting’, which is characterized by a rapid growth in flow separation near the airfoil leading edge and results in the failure of the separated shear layer to reattach to the surface of the airfoil. The suction collapse in the presence of the BL-trip is observed, arrow ‘H''’ in Fig. 8 e), to occur at a lower angle of attack as compared to the suction collapse for the clean airfoil. The lower stall angle of attack for the tripped airfoil in comparison with the clean one, as indicated in Fig. 6 a), results from this early collapse in suction caused by the addition of the BL-trip. The growth of perturbations associated with the unstable separated shear layer, following leading-edge suction collapse, results in the roll up and formation of a coherent vortical structure. This, initially small, DSV creates a distinct imprint on the C_p distribution, as indicated by arrow ‘H'’ in Fig. 8 g).

Upon emergence, the DSV grows rapidly in size, creating a large-scale suction region that extends to almost 60% of the chord on the upper surface of the airfoil at α = 22.53 deg, as shown in Fig. 8 h). The large extent of the DSV-induced suction is responsible for the distinct increase in the slope of the $C_l(\alpha)$ curve, which was observed previously in Fig. 6 a). The spatial growth of the DSV is also accompanied by the downstream convection of the vortex core which creates a distinct suction imprint on the C_p contour, as indicated in Fig. 7. The motion of the DSV core can also be inferred from the downstream displacement of the C_p suction peak with increasing α, as seen in Fig. 8 h) and i). In addition to moving downstream, the core of the DSV also convects away from the surface of the airfoil, causing the magnitude of suction to diminish gradually with increasing angles of attack. Finally, the evolution of C_p with α for $x/c \geq 0.153$ is associated with a transient, but distinct increase in C_p prior to the appearance of the DSV-induced suction imprint, as indicated by arrow ‘D’ in Fig. 7. This transient increase in C_p has also been observed in simulations, and is caused by flow entrainment towards the airfoil surface due to the DSV.

Surface Pressure Unsteadiness and Time-Frequency Signature

The root-mean-square of the surface pressure measurements was calculated, based on the local low-pass filtered, time-dependent mean, in order to obtain a basic quantitative estimate of the degree of local unsteadiness in C_p. The knowledge of unsteadiness associated with $C_p(x,\alpha)$ in turn helps in understanding the unsteady behavior of the near-wall flow field. A two-dimensional surface plot displaying the evolution of $C_{p,rms}$ with angle of attack for the clean airfoil at Re_c = 0.5×10^6 is presented in Fig. 9 a). Individual surface $C_{p,rms}$ distributions, also corresponding to the clean airfoil configuration, are presented in Fig. 10 for select angles of attack. For comparison, the $C_{p,rms}$ distributions for the tripped airfoil at α = 11.11 deg and 14.15 deg are presented along with the corresponding clean airfoil results, as shown in Fig. 10 b) and c). Similar to the C_p results, the location of the pressure transducers on the airfoil surface have also been indicated in the $C_{p,rms}$ results presented in Fig. 9 and Fig. 10.

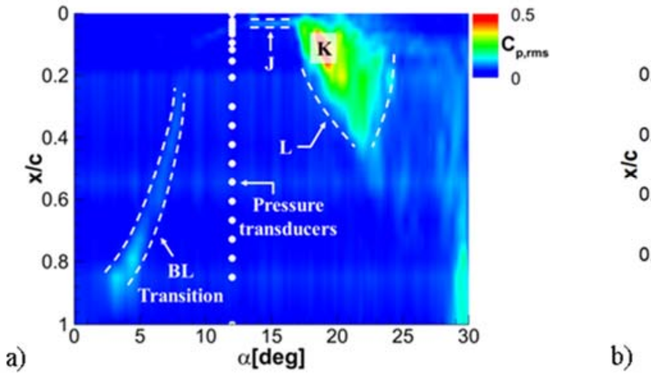

Fig. 9 a) Variation in $C_{p,rms}$ across the airfoil upper surface, and b) Approximate location of BL-transition as a function of angle of attack at $Re_c = 0.5 \times 10^6$.

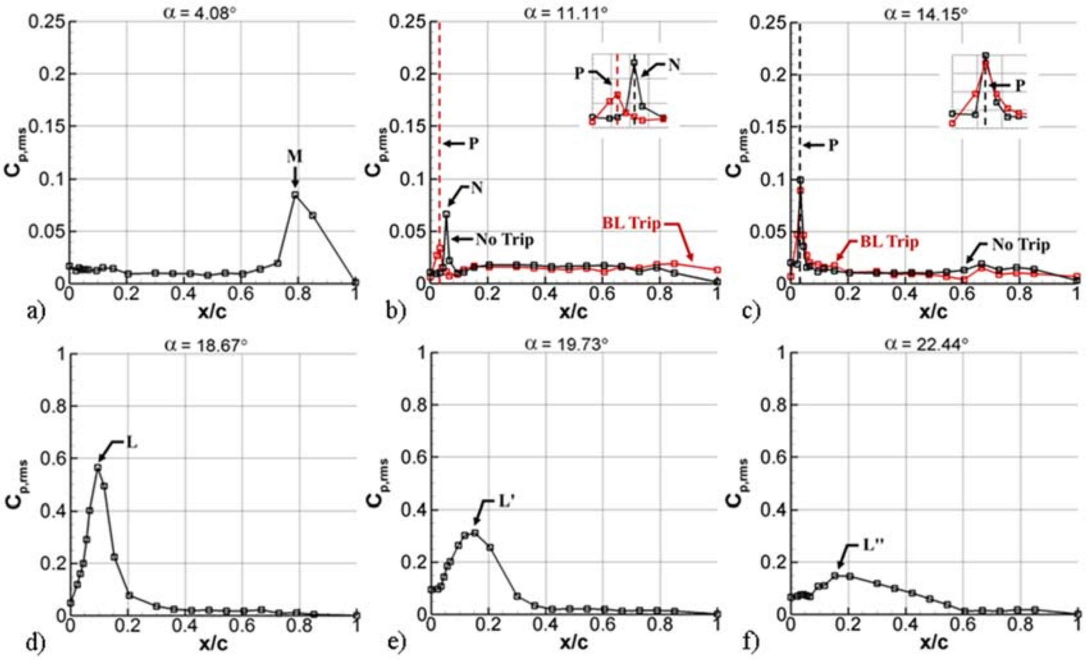

Fig. 10 Individual $C_{p,rms}$ distributions across the airfoil upper surface at a) α = 4.08 deg, b) α = 11.11 deg, c) α = 14.15 deg, d) α = 18.67 deg, e) α = 19.73 deg, and f) α = 22.44 deg, for $Re_c = 0.5 \times 10^6$.

Prior to leading-edge suction breakdown, the upstream movement of BL-transition can be inferred from the localized peaks in the $C_{p,rms}$ field, as indicated in Fig. 9 a). The approximate location of the $C_{p,rms}$ peaks, which actively display the movement of transition, as a function of the angle of attack is shown in Fig. 9 b). The local increases in $C_{p,rms}$ and the corresponding laminar-turbulent transition of the BL has also been observed in simulations. For an example $C_{p,rms}$ distribution at $\alpha = 4.08$ deg, the transition of the BL can be observed close to the airfoil trailing edge, as indicated by arrow 'M' in Fig. 10 a). At $\alpha = 11.11$ deg, a distinct $C_{p,rms}$ peak is observed near the leading edge of the clean airfoil at $x/c = 0.056$, as indicated by arrow 'N' in Fig. 10 b). This increase in $C_{p,rms}$ is caused by the turbulent reattachment of the LSB that forms in the vicinity of the airfoil leading edge, as described previously. The $C_{p,rms}$ peak moves upstream, following the reattachment point of the spatially contracting LSB, as inferred from arrows 'N' and 'P' in Fig. 10 b) and c).

For the tripped airfoil, however, a local peak in $C_{p,rms}$ appears at $x/c = 0.033$ for $\alpha = 11.11$ deg. This peak $C_{p,rms}$ position remains independent of the angle of attack, indicating a fixed BL-transition location, as shown by arrow 'P' in Fig. 10 b) and c). For the clean airfoil, the size of the LSB beyond $\alpha \approx 13$ deg was shown, in Fig. 7 b), to remain largely independent of the angle of attack. The fixed BL-transition location, as a consequence of the spatial independence of the LSB, produces a persistent region of increased $C_{p,rms}$ near the airfoil leading edge, as shown by arrow 'J' in Fig. 9 a). The LSB breakdown and the DSV formation phases of the dynamic stall process are associated with significant increases in $C_{p,rms}$, as outlined by region 'L' in Fig. 9 a). This broad region of increased $C_{p,rms}$ is also indicated by arrow 'L' in Fig. 10 d). The highest $C_{p,rms}$ magnitude is observed between $18.6 \text{ deg} \leq \alpha \leq 19$ deg, which is highlighted by the letter 'K' in Fig. 9 a). After emergence of the DSV, the magnitude of $C_{p,rms}$, however, is observed to decrease gradually, shown by arrows 'L'' and 'L''' in Fig. 10 e) and f), as the DSV core moves away from the surface of the airfoil.

The frequency content of unsteadiness associated with surface C_p was evaluated from the high frequency pressure measurements acquired between $0.023 \leq x/c \leq 0.153$, using wavelet transform methods. A contour of the phase-averaged time-dependent frequency spectra for the clean airfoil at $x/c = 0.067$ is presented in Fig. 11 a). The corresponding phase-averaged unsteady C_p evolution at $x/c = 0.067$ is also presented in Fig. 11 a), for comparison. Additionally, the time-frequency C_p spectra and the C_p evolution for the tripped airfoil, also acquired at $x/c = 0.067$, is presented in Fig. 11 b). The clean airfoil C_p spectra is associated with two distinct regions of elevated spectral amplitude across a broad range of frequencies, as shown in Fig. 11 a). The increased spectral amplitude within region '1' in Fig. 11 a) is caused by the passage of the turbulent reattachment point corresponding to the LSB. The movement of the LSB reattachment point is identified from the distinct 'bump' in the C_p curve, as indicated by arrow 'E', in Fig. 11 a). This feature is not observed for the tripped airfoil results presented in Fig. 11 b) due to the absence of the LSB formation process. In contrast, the increased spectral amplitude within region '2' is consistent across both the clean and the tripped airfoil configurations, as shown in Fig. 11 a) and b). This second region of elevated C_p unsteadiness corresponds primarily to the collapse of leading edge suction and the inception of the DSV.

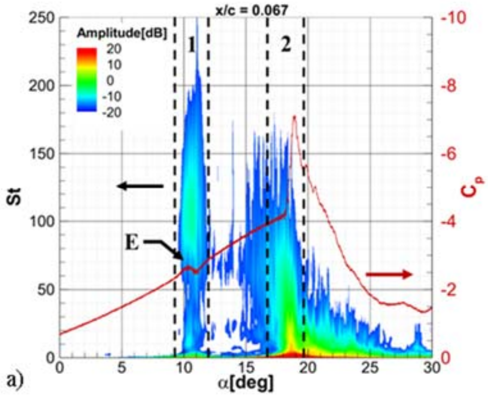

Fig. 11 Phase-averaged unsteady C_p and time-frequency C_p spectra at x/c = 0.067 for the a) 'clean' and b) 'tripped' airfoil configurations, for $Re_c = 0.5 \times 10^6$.

In an effort to identify the frequency of the dominant mode of instability associated with the LSB, an individual spectral distribution was extracted at α = 10.50 deg. This angle of attack corresponds approximately to the center of region '1' within the C_p spectra presented in Fig. 11 a). As described previously, this region corresponds to the movement of the LSB reattachment point and is, therefore, associated with unsteadiness emerging directly from the LSB. From Fig. 12 a), the C_p spectral distribution at α = 10.50 deg is characterized by a broad range of distinctly amplified frequencies around a well-defined peak. The well-defined central peak frequency corresponds to a chord-based $St \approx 100$.

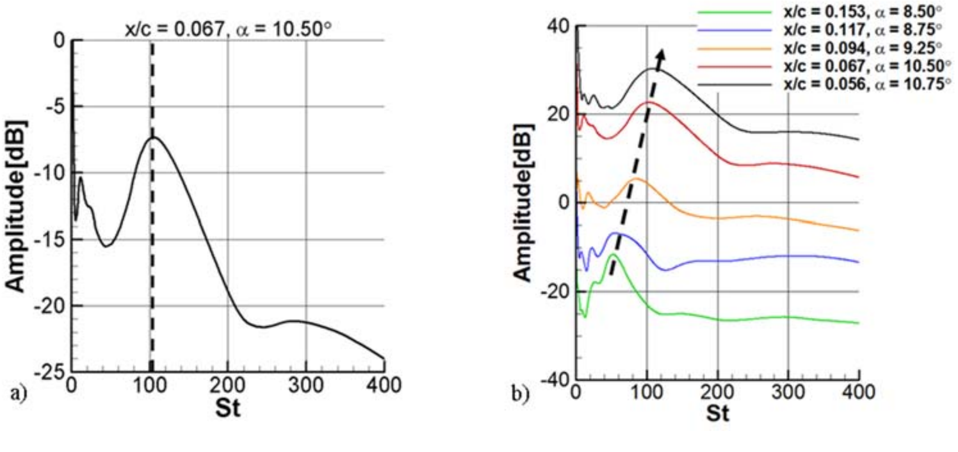

Fig. 12 Spectral lines of unsteady C_p corresponding to x/c = 0.067 at a) α = 10.50 deg, and b) 17.51 deg $\leq \alpha \leq$ 18.67 deg, for $Re_c = 0.5 \times 10^6$.

In addition to the spectral curve presented in Fig. 12 a), the C_p spectral distributions for four distinct chordwise positions of the LSB reattachment point between $0.067 \leq x/c \leq 0.153$ are presented in Fig. 12 b). Each of these spectral distributions was extracted at an angle of attack where the center of the amplified spectral content due to the passage of LSB reattachment was observed (e.g., α = 10.50 deg in Fig. 11 a)) at that given x/c location. These spectral distributions actively display the evolution of the characteristic frequencies of shear-layer instability modes due to spatial contraction of the LSB. From Fig. 12 b), the frequency bandwidth and the center frequency of the spectral distributions are observed to increase with upstream movement of the LSB reattachment point. The range of center frequencies, between $50 \leq St \leq 110$ is found to be consistent with computational studies from the literature. Thus, a spatial contraction of the LSB is accompanied by a decrease in the time scales associated with the unsteadiness in C_p. In addition to the airfoil chord length, the size of the LSB, projected on a vertical plane, was also used as a characteristic length scale for the calculation of Strouhal numbers associated with the spectral center frequencies. The variable length scale, h_{LSB}, used for the new Strouhal number calculation is given by,

$$h_{LSB} = l_{LSB}\ sin(\alpha) \tag{5}$$

where l_{LSB} is the size of the LSB along the airfoil chord, which was estimated by the distance from the leading edge to the reattachment location. Using the length scale definition from Eq. 5, the center frequencies from Fig. 12 b) were found to collapse to a single $St_{LSB} \approx 1.2$, as shown in Fig. 13 a).

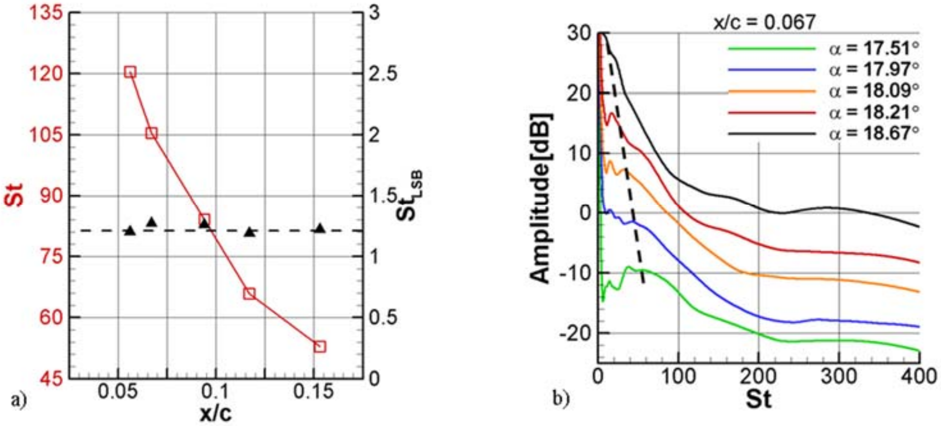

Fig. 13 a) Individual C_p spectral distributions corresponding to different chordwise positions of the LSB reattachment point, and b) center frequency scaling associated with the formatino of the DSV ($Re_c = 0.5 \times 10^6$).

In addition to analyzing the spectral content corresponding to the reattachment of the LSB, individual spectral distributions were also extracted from the clean C_p spectra at $x/c = 0.067$ across a broad range of angles of attack between $17.25 \text{ deg} \leq \alpha \leq 19$ deg, as shown in Fig. 13 b). From Fig. 13 b), the frequencies corresponding to the amplified modes of unsteady C_p are observed to decrease with increasing angles of attack. This distinctive collapse of the spectral energy towards the lower frequencies is indicative of rapid growth in the length scales of unsteadiness in C_p with increasing angles of attack, as the unsteady separation leads to the formation of the DSV.

Off-body Flow Field Evolution

In addition to the unsteady surface pressure measurements, which were used to examine the evolution of the BL and the near-wall flow field, TR-PIV data were also acquired to understand the global flow behavior across a broad spatial region next to airfoil upper surface. The phase-averaged *z*-vorticity contours displaying the emergence and formation of the DSV at $Re_c = 0.5 \times 10^6$ across select angles of attack are presented in Fig. 14. The variations in C_l with respect to the angle of attack at $\alpha = 17.97$ deg, 19.75 deg, and 22.53 deg, are also provided in Fig. 14, for reference. Additionally, the phase-averaged scalar velocity field contours, non-dimensionalized with respect to the freestream velocity, at $\alpha = 20.63$ deg, 22.53 deg, and 23.72 deg are shown in Fig. 15. These velocity field results are used to complement the physical understanding gained from observing the evolution of the vorticity field with changes in angle of attack. In addition to the phase-averaged flow fields, contours of the instantaneous Q-criterion, also selected at $\alpha = 20.63$ deg, 22.53 deg, and 23.72 deg, are presented in Fig. 16, for direct comparison with the phase-averaged results. The instantaneous *z*-vorticity field is also provided in Fig. 16 a), along with the corresponding Q-criterion contour at $\alpha = 20.63$ deg. All of the vorticity results presented in this article were normalized through a global min-max normalization process. Furthermore, a thresholding filter was also employed to set the vorticity below a specified value to zero. The thresholding value was judiciously chosen to eliminate the inconsequential background vorticity whilst effectively enhancing the visibility of the vorticity development associated with the flow structures of interest. All of the TR-PIV results presented in this section were acquired at a Reynolds number of $Re_c = 0.5 \times 10^6$ and correspond to the clean airfoil configuration.

At $\alpha = 17.97$ deg, the flow around the airfoil is observed to be largely irrotational, except for a narrow region of concentrated vorticity in the immediate vicinity of the upper surface of the airfoil, as indicated by arrow 'Q' in Fig. 14 a). The significant thickening of the region of high vorticity concentration towards the airfoil trailing edge is indicative of trailing-edge flow separation, which results in reduced pressure recovery across the aft portion of the airfoil, as indicated previously in Fig. 8 e). It should be specified that the vorticity contour presented in Fig. 14 a) corresponds to an angle of attack at which the magnitude of leading-edge suction of the airfoil was observed, from Fig. 7 a), to attain a global maximum. Furthermore, the angle of attack associated with the flow in Fig. 14 a), is also significantly larger than the static stall angle of attack of the airfoil at $Re_c = 0.5 \times 10^6$. Thus, consistent with the classical understanding of dynamic stall, the flow around the NACA 0012 airfoil undergoing a dynamic pitch maneuver is associated with significant delay in stall, as evidenced by the large flow field irrotationality and peak suction magnitude, in comparison with static variations in the angle of attack. Increasing the airfoil angle of attack to $\alpha = 19.29$ deg is accompanied by the appearance of a localized region of high vorticity magnitude in the vicinity of the leading edge of the airfoil, as indicated by arrow 'R' in Fig. 14 b).

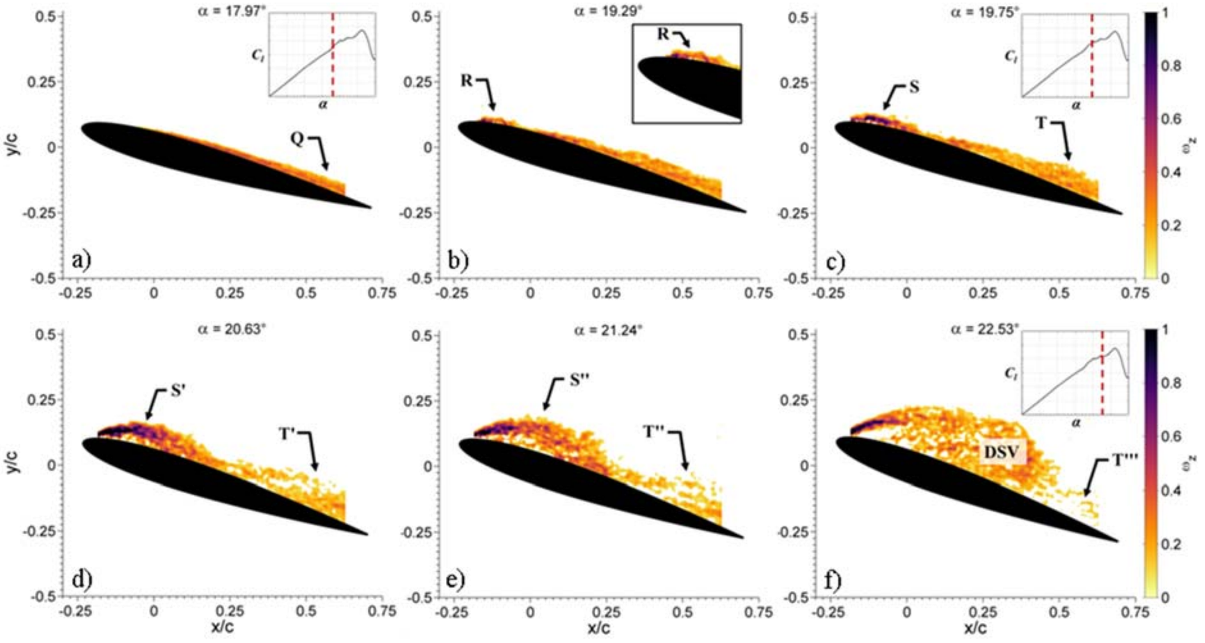

Fig. 14 Phase-averaged z-vorticity contours at a) α = 17.97 deg, b) α = 19.29 deg, c) α = 19.75 deg, d) α = 20.63 deg, e) α = 21.24 deg, and f) α = 22.53 deg, for $Re_c = 0.5 \times 10^6$.

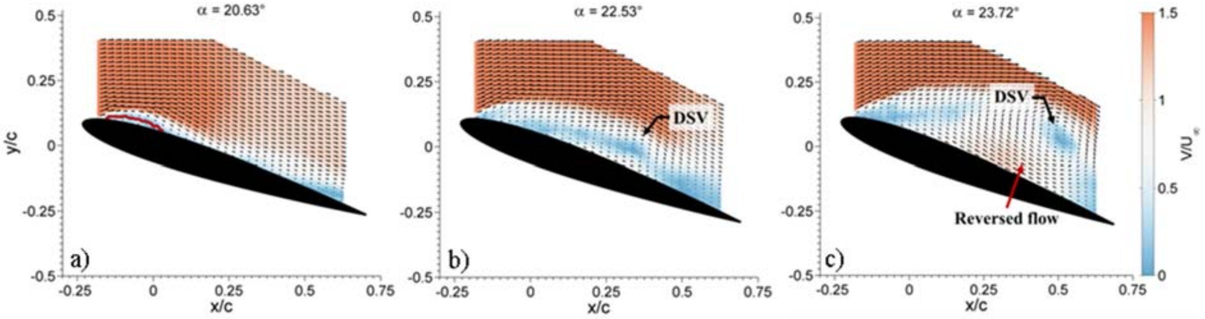

Fig. 15 Phase-averaged scalar velocity contours at a) α = 20.63 deg, b) α = 22.53 deg, and c) α = 23.72 deg, for $Re_c = 0.5 \times 10^6$.

With further increase in the angle of attack, the initially localized region of vorticity grows rapidly, resulting primarily from the strong vorticity generation at the leading edge of the airfoil. This spatial growth in vorticity is indicated by arrows ‘S’, ‘S'’, and ‘S"’ in Fig. 14 c), d), and e), respectively. The rapid increase in circulation near the airfoil leading edge is accompanied by a phase of non-linear growth in the airfoil C_l, as observed from the $C_l(\alpha)$ distribution presented in the inset of Fig. 14 c). During this phase of the dynamic stall process, the leading-edge boundary layer separates from the airfoil surface, forming a rapidly growing region of reversed flow, as outlined by the red curve in the velocity field contour at α = 20.63 deg presented in Fig. 15 a). The reduced curvature of the flow near the airfoil leading edge, after separation, causes a rapid decline in the magnitude of suction. This collapse in suction, following the breakdown of the

LSB, had been observed previously in the C_p distribution presented in Fig. 8 f). At $\alpha = 20.63$ deg, the high leading-edge vorticity concentration extends up to $x/c \approx 0.5$, leading to a significant entrainment of the freestream towards the airfoil surface, as observed immediately downstream of the region outlined in red, in Fig. 15 a). The freestream entrainment towards the airfoil is accompanied by a gradual downstream displacement of the reversed flow region that was produced originally by trailing-edge separation from the airfoil surface. This phenomenon is further accompanied by a rapid decline in the vorticity concentration, presumably due to viscous diffusion, with increasing angles of attack, as indicated by arrows ‘T’, ‘'T'’, and ’T"’ in Fig. 14 d), e) and f), respectively.

The region of concentrated vorticity, arrow ‘S'’ from Fig. 14 d), is associated with a stochastic distribution of coherent vortical structures as observed from the instantaneous Q-criterion and z-vorticity (inset) contours, shown in Fig. 16 a). Thus, the instantaneous flow field, at the transitional Reynolds number, is characterized by a range of fine-scale structures due to the presence of a wide spectrum of length and time scales in the flow. This observation is in contrast with the phase-averaged flow fields that are more reminiscent of the classical understanding of DSV morphology. The small-scale, coherent structures are conjectured to result from a Kelvin-Helmholtz type instability of the separated shear layer, and will be examined in greater detail using linear stability analysis and modal decomposition methods described in the following sections. It should be mentioned here that the irregular nature of the instantaneous TR-PIV flow fields is not an artifact of the PIV processing methodology, but an actual representation of the true behavior of the flow around the airfoil. The statistical nature of the instantaneous flow is, however, significantly diminished during the phase averaging process resulting in a well-organized flow behavior observed in Fig. 14 and Fig. 15.

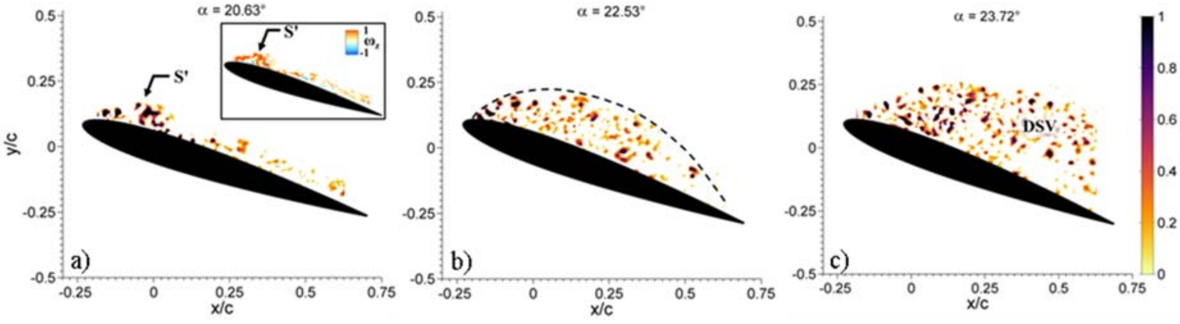

Fig. 16 Contours of instantaneous Q-criterion at a) $\alpha = 20.63$ deg, b) $\alpha = 22.53$ deg, and c) $\alpha = 23.72$ deg, for $Re_c = 0.5 \times 10^6$.

Near the airfoil leading edge, the complex, non-linear interactions within the high vorticity region of the flow eventually lead to the formation of a coherent dynamic stall vortex. This DSV, upon emergence, is identified clearly in the phase-averaged and instantaneous TR-PIV results presented in Fig. 14–Fig. 16. The emergence of the DSV is associated with a broad region of increased suction across the airfoil upper surface, as observed previously in the C_p distributions presented in Fig. 8. Additionally, this phase of the dynamic stall process also coincides with the rapid increase in the lift curve slope, as can be seen from the $C_l(\alpha)$ inset presented in Fig. 14 f). Consistent with the nature of the instantaneous flow fields described earlier, the DSV from Fig. 16 is observed to consist of a multitude of small-scale vortical structures. This instantaneous, fine-grained nature of the DSV is also consistent with recent experimental studies in literature.

After formation, the DSV is observed to convect downstream with increasing angles of attack. The entrainment of the surrounding fluid by the DSV causes it to grow rapidly in size, creating a region of strong reversed flow next to the airfoil surface, as indicated in Fig. 15 c). The rapid spatial growth of the DSV, in turn, causes a gradual displacement of the vortex core away from the surface of the airfoil. The combination of the streamwise and transverse movements of the DSV with increasing angles of attack can be inferred clearly by comparing the velocity field results from Fig. 15 b) and c). The behavior of the DSV from TR-PIV measurements is consistent with the behavior that was conjectured from the surface pressure field evolution presented in Fig. 7 and Fig. 8. Finally, the velocity field after the convection of the DSV past the trailing edge of the airfoil, not shown here for brevity, is characterized by post-stall bluff-body wake with a large recirculation region.

Time-Frequency Signature from TR-PIV

In addition to the off-body flow development described in the section above, the time-dependent dominant frequencies and corresponding amplitudes of oscillations within the unsteady flow field were also extracted from the velocity measurements acquired using TR-PIV. A multivariate, multi-dimensional empirical mode decomposition (EMD) technique coupled with a Hilbert transform approach was used for the extraction of the aforementioned physical quantities. The EMD processing technique was deemed as an appropriate choice for the decomposition of the velocity field, since the non-linear, non-stationary dynamic stall process of the present investigation does not readily comply with a pre-defined set of basis functions. The multi-dimensional, multivariate approach ensures that the modal components of the velocity field retain coherence on multiple velocity components (i.e., u and v), and across multi-dimensional space time (i.e., x, y, and t). An example velocity field and the corresponding EMD-derived IMFs at $\alpha = 21.24$ deg and $Re_c = 0.5 \times 10^6$, are presented in Fig. 17 a) – e). The Residue of the velocity field, which represents the background trend of the non-stationary dynamic stall process, is also presented in Fig. 17 f). From Fig. 17, a gradual increase in the length scale, and by extension the time-period of oscillations in the flow, can be observed with increasing IMF number. Thus, IMF 1 displays the smallest scales contained within the separated shear layer that could be resolved with the present TR-PIV measurements. As such, the flow structures represented by IMF 1 are still significantly larger than the Kolmogorov scale of the turbulent flow field. In contrast with IMF 1, IMF 4 represents the larger, streamwise-oriented streaks in the flow, as observed in Fig. 17 e). It should be mentioned here that this progression of scales is not coincidental but follows from the EMD methodology, wherein the highest frequencies contained within a signal are by design, associated with the lowest IMF.

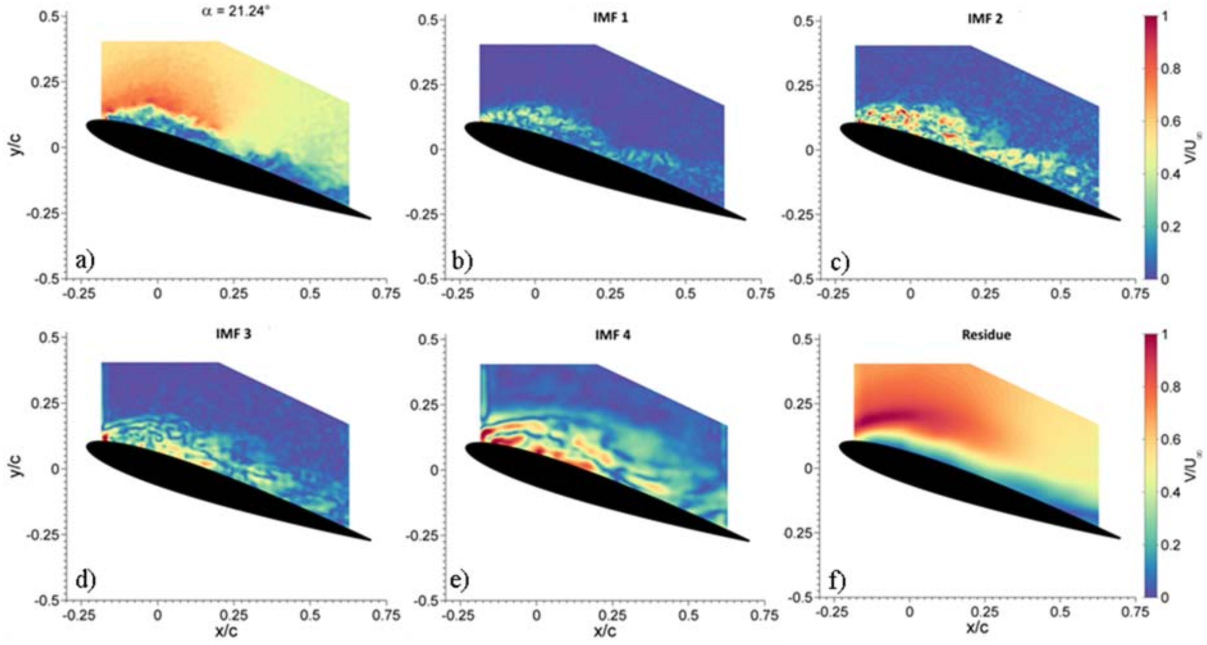

Fig. 17 Instantaneous velocity field contour at *α* = 21.24 deg along with IMF 1-4 and Residue, extracted using EMD at the corresponding angle of attack. (*Re*$_c$ = 0.5 × 10^6)

The instantaneous amplitude and frequency fields were calculated for each IMF at various angles of attack using the Hilbert transform method, as mentioned previously. The spatial distribution of power, calculated as the square of amplitude, associated with the oscillations in the velocity field for IMF 1, 2, and 3 at *α* = 21.24 deg, is presented in Fig. 18. These power levels help in the identification of the time-dependent dominant oscillatory content in the flow. From Fig. 18, the separated shear layer is observed to contain high amplitude oscillations near the leading edge of the airfoil. The peak power associated with these oscillations is observed to decrease with increasing IMF number, with IMF 1 being associated with the most amplified oscillations in the flow at *α* = 21.24 deg.

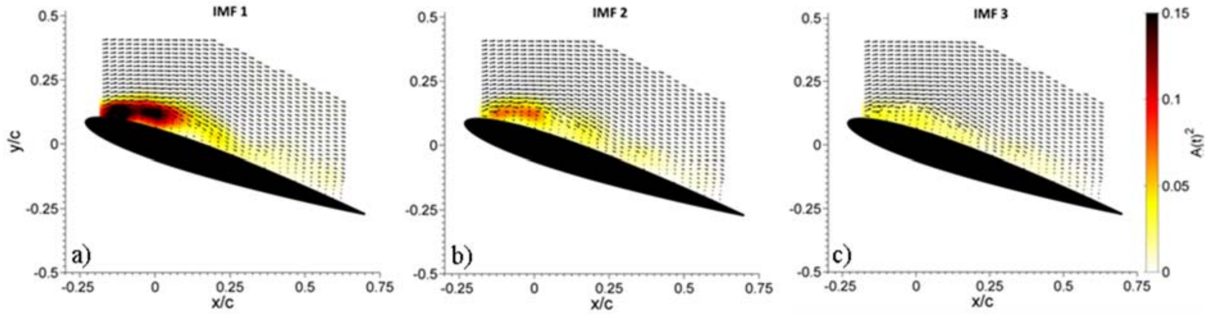

Fig. 18 Contours of the instantaneous power distribution for the first three IMFs at *α* = 21.24 deg, for *Re*$_c$ = 0.5 × 10^6.

The dominant frequencies in the flow, which are defined as the frequencies associated with the highest oscillation amplitude at each point in space, are presented in Fig. 19, for several representative angles of attack. It is important to note that the frequencies in Fig. 19 were obtained by phase averaging the instantaneous frequencies over several experimental realizations. The phase-averaged frequencies were then further processed through a median based filter to identify and effectively eliminate any spurious results from the more physically-representative spatial frequency distribution. The amplitude of oscillation, and consequently the oscillatory power, is also represented in Fig. 19, by the level of transparency of the color map associated with the frequency distribution in the flow. Thus, the less dominant frequencies are colored more transparently than the more powerful oscillations in the flow field. From Fig. 19, the separation of the boundary layer from the airfoil leading edge is accompanied by a rapidly-growing region of high frequency oscillations in the flow field. These high frequency oscillations are observed to move with the separated shear layer as it is displaced away from the airfoil surface. A pair of red curves are superimposed over the frequency contours presented in Fig. 19. These red curves outline the region of the flow where the oscillatory power for a given *x/c* location is greater than 85% of the maximum power at that *x/c* location. Similar to the high-frequency region observed in IMF 1 and 2, the red curves are also observed to straddle the separated shear layer, which indicates that the highest amplitudes of oscillations in the flow are contained within this separated shear layer. This feature of the current dynamic stall process at $Re_c = 0.5 \times 10^6$ was also highlighted previously in Fig. 18.

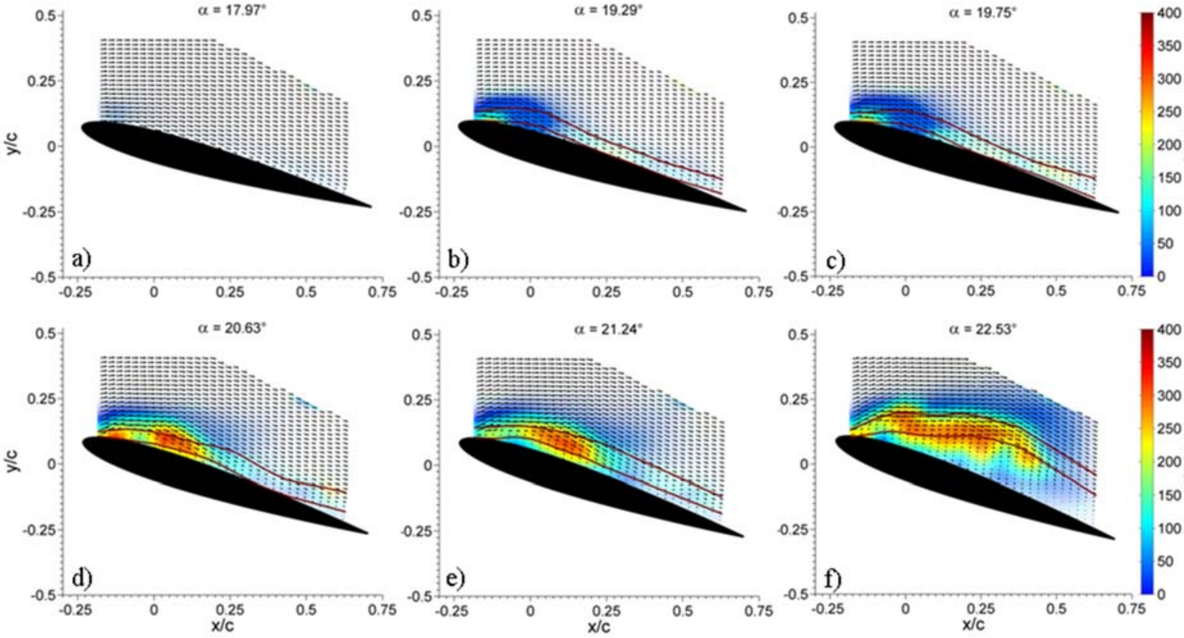

Fig. 19 Contours of the phase-averaged frequencies associated with the highest amplitude oscillations in the flow at select angles of attack, for $Re_c = 0.5 \times 10^6$.

The mean of the dominant frequencies and the associated power in the region that is highlighted by the red curves in Fig. 19, was extracted for each *x/c* location and for a range of angles of attack. Contours of the evolution of the mean power and the mean oscillatory frequencies are presented in Fig. 20. A threshold filter is employed in these plots to blank regions where the power associated with the velocity fluctuations is lower than a pre-defined threshold power level, in order to help enhance visibility of the dominant modes of oscillations that are of interest. The angle of attack corresponding to the rapid growth in leading-edge vorticity, identified previously from Fig. 14, is highlighted by the dashed line containing the acronym 'LEV' in Fig. 20. Additionally, the angle of attack corresponding to the emergence of the DSV is also highlighted by a dashed line in Fig. 20. From Fig. 20 a), the amplitude of oscillation in the velocity field is observed to grow rapidly during the emergence of leading-edge vorticity, and occurs prior to the emergence of the DSV. This observation is consistent with the rapid growth in $C_{p,rms}$ which was observed during the LSB breakdown phase of the dynamic stall process, as highlighted in Fig. 9 a). The rapid increase in unsteadiness prior to the emergence of the DSV is also consistent with a number of computational studies in the literature. The 'high $A(t)^2$' regions outlined by the dashed curves in Fig. 20, defines a region in the contour plot where the power associated with the velocity field oscillations is greater than two standard deviations above the global mean power level. Thus the highest degree of unsteadiness in the velocity field, from Fig. 20, is observed to be concentrated near the leading edge of the airfoil. The growth of LEV and the accompanied separation of the boundary layer, leads to the appearance of high frequency oscillations ($f \approx 275$ Hz) in the velocity field, as had been observed previously in Fig. 19. These dominant high frequency oscillations are observed, from Fig. 20 b), to be initially concentrated near the upstream half of the airfoil. After the emergence of the DSV however, higher frequency modes begin to appear in the velocity field near the aft region of the airfoil, arrow 'HF' in Fig. 20 b), albeit with significantly lower amplitudes, in comparison with the leading-edge region during the LEV phase of the dynamic stall process.

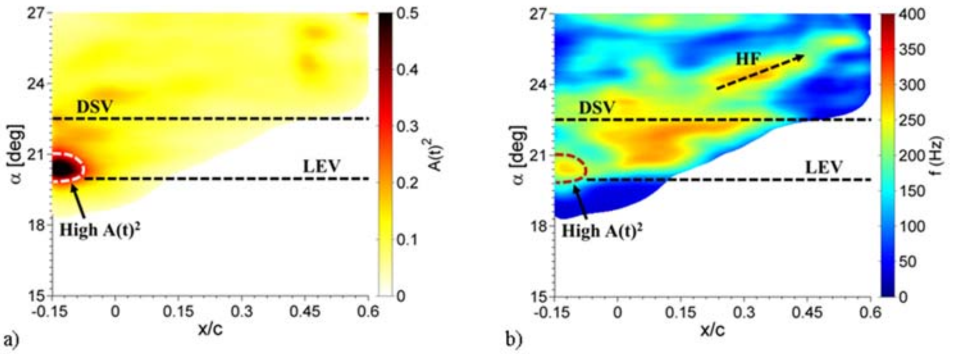

Fig. 20 Contours of the variation in the a) mean power and b) mean oscillatory frequencies associated with the spatial region between the red curves (from Fig. 19), as a function of *x/c* and the airfoil angle of attack at $Re_c = 0.5 \times 10^6$.

Influence of Reynolds Number

In order to understand the effects of the variation in the viscous time scale on the dynamic stall process, experiments were also performed at $Re_c = 0.2 \times 10^6$ and 1×10^6, for the clean airfoil configuration. A set of experiments were also performed recently at a significantly lower Reynolds number of $Re_c = 0.010 \times 10^6$. These results, aimed at understanding the effects on the dynamic stall process due to a two orders of magnitude variation in the Reynolds number, are currently being processed and will be presented in a future publication. The characteristic features of flow evolution acquired at these additional Reynolds numbers are compared against the $Re_c = 0.5 \times 10^6$ results, described previously. It should be specified here that the experimental data for all the aforementioned Reynolds numbers were acquired for a linear ramp motion profile at $\omega^+ = 0.05$ and across a common angle of attack range, $-5 \text{ deg} \leq \alpha \leq 30 \text{ deg}$. Thus, any characteristic differences in the dynamic stall process are expected to result solely from the variation in the Reynolds number.

Off-body Flow Field Evolution

The flow evolution during the initial stage of the airfoil motion, characterized primarily by trailing-edge separation, not shown here for brevity, is found to be consistent across all the Reynolds numbers. With further increase in the angle of attack, an abrupt leading-edge flow separation event, along with rapid growth in leading-edge vorticity, is also observed across all three Reynolds numbers. For $Re_c = 0.2 \times 10^6$, the spatial growth in leading-edge vorticity with increasing angles of attack leads eventually to the formation of the DSV, as seen in Fig. 21. This process of the formation of the DSV, coupled with rapid vorticity dissipation near the trailing-edge region of the airfoil, is similar to the dynamic stall process that is observed at $Re_c = 0.5 \times 10^6$, as was described previously from Fig. 14.

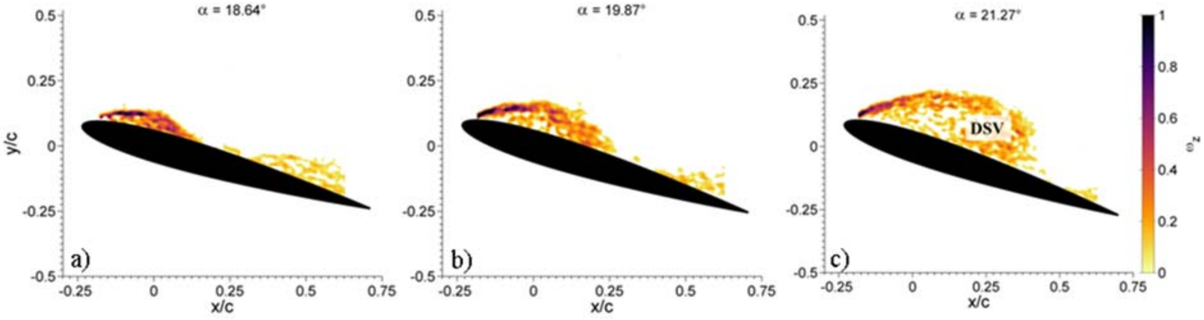

Fig. 21 Phase-averaged z-vorticity contours at a) $\alpha = 18.64$ deg, b) $\alpha = 19.87$ deg, and c) $\alpha = 21.27$ deg, for $Re_c = 0.2 \times 10^6$.

In contrast with the flow evolution at $Re_c = 0.2 \times 10^6$ and $Re_c = 0.5 \times 10^6$, the boundary-layer separation from the airfoil leading edge at $Re_c = 1.0 \times 10^6$ is rapidly followed by the coalescence of vorticity across the airfoil upper surface into two distinct regions. These coherent vortical structures are indicated by arrows 'V_1' and 'V_2' in Fig. 22 a). The formation of the primary vortex, 'V_1', is characteristically similar to that of a traditional leading-edge vortex, as had been observed previously at $Re_c = 0.5 \times 10^6$, shown in Fig. 14. The emergence of the secondary vortex, 'V_2', however, results from the roll up of the shear layer vorticity aft of $x/c \approx 0.125$, and reflects a significant departure from the classical dynamic stall process which is usually characterized by the formation of a single DSV. After the formation of the vortex pair, the secondary vortical structure, 'V_2', is observed from Fig. 22 a) and b), to gradually merge with the leading-edge vortex, 'V_1'. During this complex co-rotating vortex merging process, the vorticity contained within the two, initially distinct vortical structures, is redistributed into a single, coherent DSV, as observed in Fig. 22 c). This vortex merging process and DSV emergence can be identified more clearly from the ‘attracting’ ridges of the n-FTLE contours presented in Fig. 23. Much of the vortex dynamics associated with $Re_c = 1.0 \times 10^6$, described in this section, is consistent with the computational results of Benton and Visbal [19]. Additionally, the time evolution of the FTLE field from Fig. 23, displays strong qualitative similarity to the corresponding topological results of Mulleners and Raffel [12].

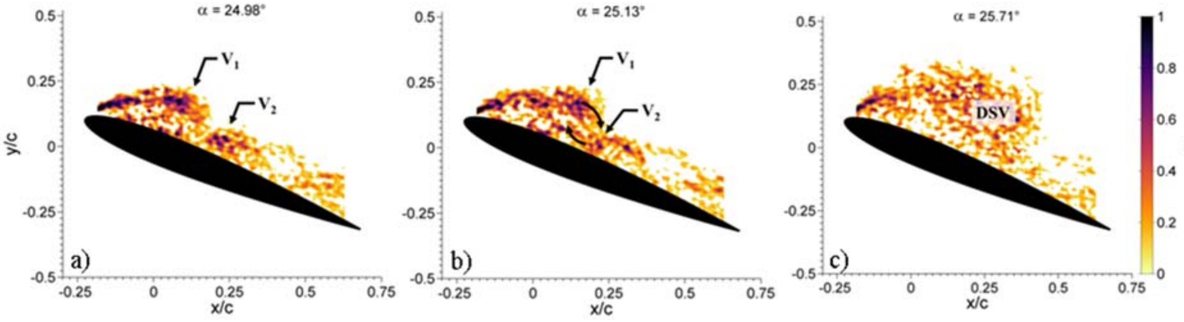

Fig. 22 Phase-averaged z-vorticity contours at a) *α* = 24.98 deg, b) *α* = 25.13 deg, and c) *α* = 25.71 deg, for $Re_c = 1 \times 10^6$.

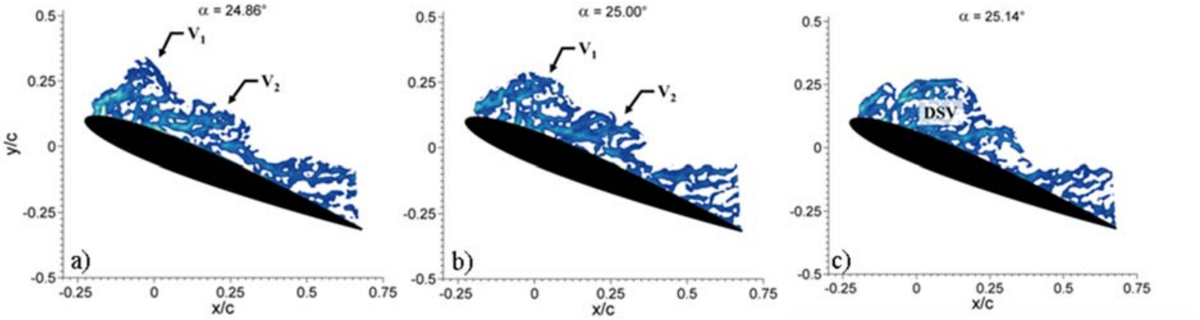

Fig. 23 Contours of the n-FTLE field at a) *α* = 24.86 deg, b) *α* = 25.00 deg, and c) *α* = 25.14 deg, for $Re_c = 1 \times 10^6$.

Time-Frequency Signature from TR-PIV

Similar to $Re_c = 0.5 \times 10^6$, the dominant frequencies and amplitudes of oscillations in the velocity field were also extracted for $Re_c = 0.2 \times 10^6$ and $Re_c = 1.0 \times 10^6$, using a coupled EMD and Hilbert transform technique. The dominant frequencies associated with the time-dependent flow field for select angles of attack at $Re_c = 0.2 \times 10^6$ and $Re_c = 1.0 \times 10^6$ are presented in Fig. 24 and Fig. 25, respectively. Consistent with Fig. 19, the relative amplitudes of oscillations at different spatial locations within the flow field are represented by the level of transparency associated with the color map that is used to describe the frequency field. The distribution of frequencies in the flow for $Re_c = 0.2 \times 10^6$ is observed, from Fig. 24, to be significantly lower in magnitude as compared to the dominant frequency distribution for $Re_c = 1.0 \times 10^6$, presented in Fig. 25. Moreover, from Fig. 25 a), two distinct regions with relatively high frequencies of significant amplitude can be observed in the flow, closer to the leading edge of the airfoil. These regions correspond to vortices ‘V_1’ and ‘V_2’, which were identified previously from the phase-averaged vorticity contours presented in Fig. 22.

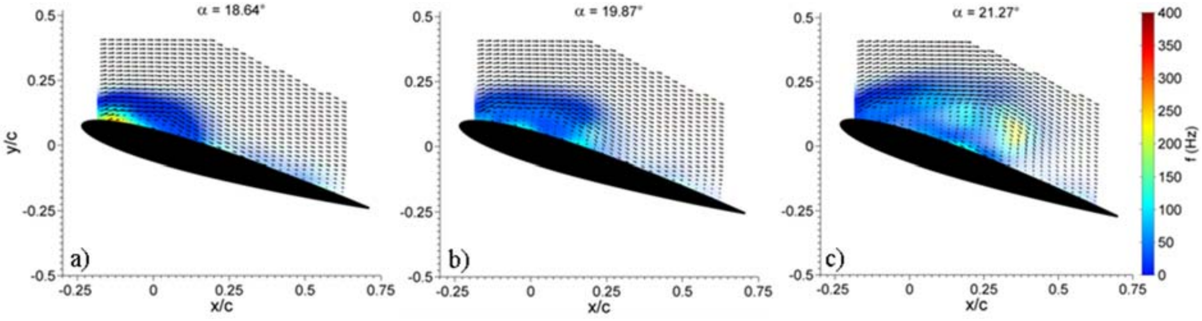

Fig. 24 Contours of the phase-averaged frequencies associated with the highest amplitude oscillations in the flow at select angles of attack, for $Re_c = 0.2 \times 10^6$.

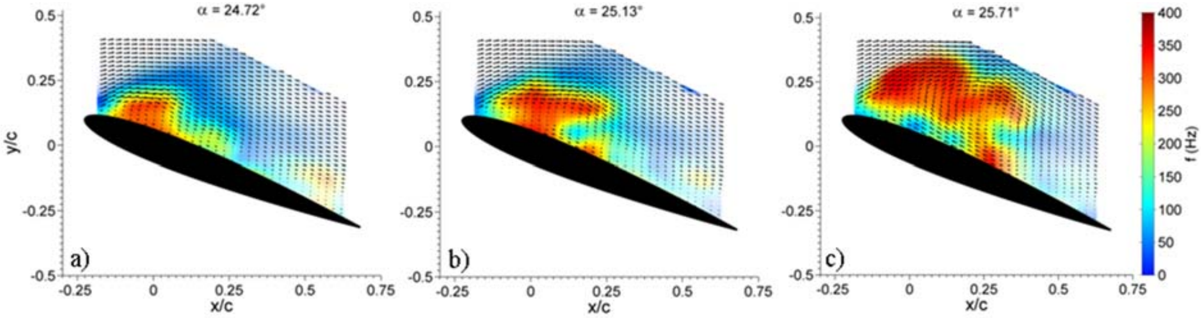

Fig. 25 Contours of the phase-averaged frequencies associated with the highest amplitude oscillations in the flow at select angles of attack, for $Re_c = 1.0 \times 10^6$.

Similar to $Re_c = 0.5 \times 10^6$, regions of the flow where the power associated with the unsteady velocity fluctuations is greater than 85% of the maximum power for each x/c location, were extracted for the $Re_c = 0.2 \times 10^6$ and $Re_c = 1.0 \times 10^6$ flow fields. The variation in the mean frequency associated with this high amplitude region as a function of the streamwise location, x/c and the angle of attack is presented in Fig. 26, for both Reynolds numbers. Similar to Fig. 20, the ‘high $A(t)^2$’ regions in Fig. 26, are associated with an oscillatory power level that is greater than two standard deviations above the global mean power level for that particular Reynolds number. Thus, the LEV events for $Re_c = 0.2 \times 10^6$ and $Re_c = 1.0 \times 10^6$, from Fig. 26, are associated with significantly high degrees of unsteadiness in the flow near the leading edge of the airfoil. This observation is consistent with the variation in the dominant mean power at $Re_c = 0.5 \times 10^6$, presented in Fig. 20 a). Traces of relatively high frequency oscillations ($f \approx 125$ Hz) at $Re_c = 0.2 \times 10^6$, can also be observed from Fig. 26 a) after the emergence of the DSV, as indicated by arrow ‘HF’. The spatial extent of these high frequency oscillations is however, significantly smaller than the high frequency regions observed at $Re_c = 0.5 \times 10^6$. In contrast with $Re_c = 0.2 \times 10^6$ and $Re_c = 0.5 \times 10^6$, an upstream progression of high oscillation frequencies, with $f \approx 225$ Hz, can be observed at $Re_c = 1.0 \times 10^6$ prior to the emergence of the LEV, as indicated by the arrow ‘HF'’ in Fig. 26 b). This observation indicates that the overall level of unsteadiness in the velocity field in the aft region of the airfoil, prior to the abrupt separation of the boundary layer, is significantly higher for $Re_c = 1.0 \times 10^6$ in comparison with $Re_c = 0.2 \times 10^6$ and $Re_c = 0.5 \times 10^6$. Even higher frequencies, $f \approx 300$ Hz, emerge near the airfoil leading edge after the LEV event at $Re_c = 1.0 \times 10^6$. These very high frequency oscillations in the velocity field grow rapidly, covering the entire chord length of the airfoil soon after the emergence of the DSV.

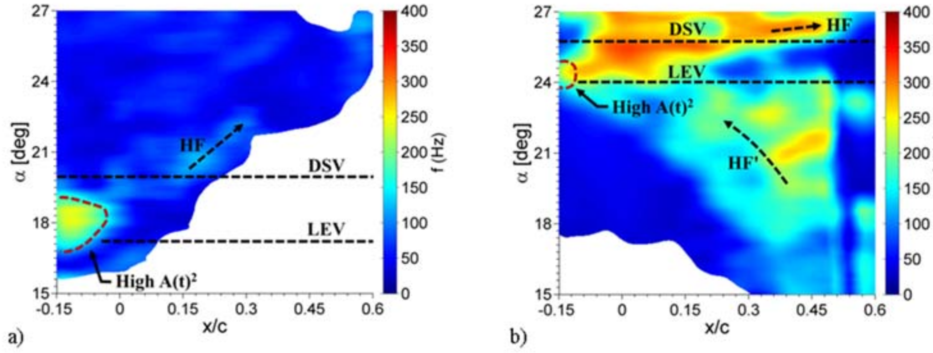

Fig. 26 Contours of the variation in the mean dominant frequencies as a function of *x/c* and the airfoil angle of attack at a) $Re_c = 0.2 \times 10^6$ and b) $Re_c = 1.0 \times 10^6$.

In addition to the experimentally determined time-frequency signature, the spatially-unstable, two-dimensional modes present within the flow field were also calculated directly from the Orr-Sommerfeld equations through a numerical procedure involving the expansion of linear perturbations in terms of a finite set of Chebyshev polynomials. The details with regards to the solution of the Orr-Sommerfeld eigenvalue problem using the Chebyshev collocation method can be found in several classic references in literature. This numerical procedure was applied to base flows which were described by the phase-averaged velocity fields at $\alpha = 18.64$ deg, $\alpha = 20.63$ deg, and $\alpha = 24.72$ deg, for $Re_c = 0.2 \times 10^6$, $Re_c = 0.5 \times 10^6$, and $Re_c = 1 \times 10^6$, respectively. It should be mentioned here that these angles of attack correspond to the initial stages of leading-edge flow separation in the overall dynamic stall process at the respective Reynolds numbers.

For each flow field, the *x*-velocity component, u/U_∞, was extracted as a function of *y/c*, for a fixed *x/c* location. A hyperbolic tangent profile was then fitted over this velocity distribution through a least-squares curve fitting procedure. The eigenvalues of the Orr-Sommerfeld operator combined with the hyperbolic tangent velocity profile were then evaluated to predict the unstable velocity perturbation modes with real frequencies, *f*, and complex wavenumbers, α_c. The imaginary part of this complex wavenumber, α_i, corresponds to the exponential growth rate of the velocity perturbations in the flow field along the streamwise direction. The variation in the perturbation growth rate, α_i, can then be studied as a function of the frequencies, *f*, which in turn assists in the prediction of the dominant mode of spatial instability in the flow field. The entire process is then repeated for a set of different base velocity profiles, extracted at several *x/c* locations within the flow, producing a contour plot of the variation in α_i as a function of the frequency, *f*, and *x/c*, for a fixed angle of attack and Reynolds number. Contours of the eigenvalue spectra of instability at three select angles of attack for each of the three Reynolds numbers is provided in Fig. 27. A thresholding filter was employed to remove the instability modes associated with inconsequentially small growth rates from the contour plots presented in Fig. 27. Additionally, the growth rate, α_i, from Fig. 27 was normalized through a global min-max normalization procedure. The velocity vectors for each of the three cases presented in Fig. 27, are superimposed over the background instability spectra, for reference. It should be mentioned here that the *y*-axis for the velocity vectors in Fig. 27 has been re-defined such that the origin for the *y*-axis at any given *x/c* location is located at the surface of the airfoil.

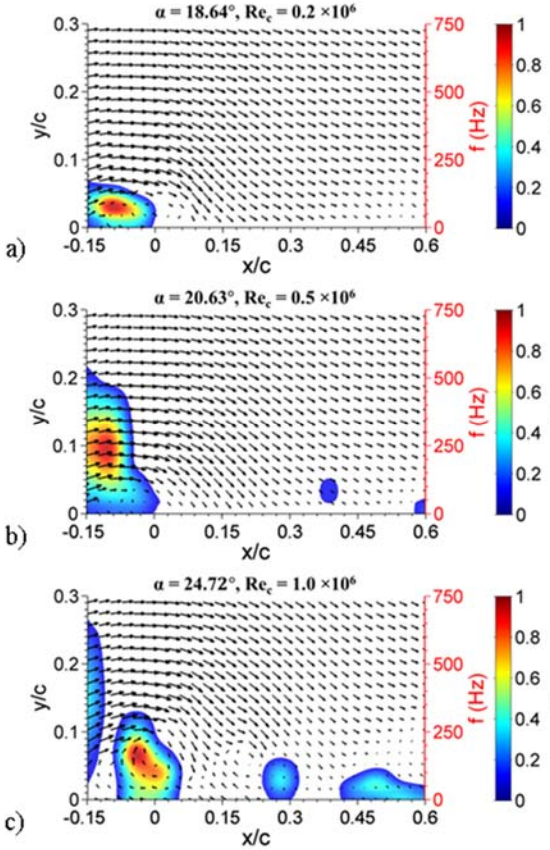

Fig. 27 Eigenvalue spectra of instability obtained from numerical solution of the Orr-Sommerfeld equation for select velocity fields at a) $Re_c = 0.2 \times 10^6$, b) $Re_c = 0.5 \times 10^6$, and c) $Re_c = 1.0 \times 10^6$.

From Fig. 27, the velocity profiles corresponding to the reversed flow region near leading-edge of the airfoil are associated with a range of unstable modes, which span a diverse range of frequencies. The normalized growth rate, α_i, for these unstable modes can be inferred from the color bar, which is presented to the right of each plot. Example eigenvalue spectral lines at $x/c \approx -0.15$, are extracted for each of the three Reynolds numbers. These eigenvalue spectral lines are presented in Fig. 28. The color bands in Fig. 28 represent the variation in the eigenvalue spectra due to a $\Delta\alpha = \pm 0.05$ deg change in angle of attack. The relatively low degree of scatter associated with the spectral lines, from Fig. 28, demonstrates that the instability profile is largely insensitive to minor variations in the base flow. Additionally, from Fig. 28, the eigenvalue spectral lines are observed to be qualitatively similar to the classical shear layer instability profiles from literature.

The frequencies associated with the highest perturbation growth rate from Fig. 28 are presented in Table 1. From Fig. 28, the dominant frequency, along with the range of unstable frequencies is observed to increase with increasing Reynolds numbers. The maximum growth rate is also observed to increase with increasing Reynolds number as viscous damping becomes increasingly insignificant as compared to the inertial-driven effects. The experimentally-determined dominant frequencies, f_e, for the corresponding angles of attack at $x/c \approx -0.15$ is also presented in Table 1. From Table 1, the experimental frequencies are observed to be largely consistent with the linear stability predictions for $Re_c = 0.2 \times 10^6$ and $Re_c = 0.5 \times 10^6$. At $Re_c = 1.0 \times 10^6$ however, the numerically-determined frequency, $f = 370$ Hz is found to be greater than the experimental counterpart, $f_e = 260$ Hz. Thus, the small-scale, high frequency modes predicted by the linear stability analysis are not realized physically for $Re_c = 1.0 \times 10^6$. However, the growth rate of $\alpha_i = 0.68$, which is observed from the $Re_c = 1.0 \times 10^6$ eigenvalue spectra in Fig. 28 for a modal frequency of $f = 260$ Hz, is only 10% smaller than the maximum growth rate of $\alpha_i = 0.76$ at $f = 370$ Hz. Thus, the linear stability analysis predictions are observed to be reasonably consistent with the experimentally-determined results across all three Reynolds numbers, for the selected angles of attack and at a streamwise location of $x/c \approx -0.15$.

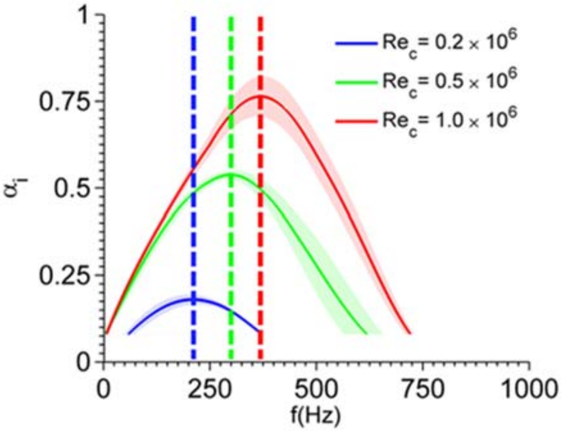

Fig. 28 Individual eigenvalue spectral lines at $x/c \approx -0.15$ for $Re_c = 0.2 \times 10^6$, $Re_c = 0.5 \times 10^6$, and $Re_c = 1.0 \times 10^6$.

A shear layer displacement thickness based Strouhal number was calculated from the dimensional frequencies presented in Table 1, for both the experimental, $St_{\delta,e}$, and the numerically-derived, St_δ, results. The disparate set of frequencies across the three Reynolds numbers reported in this study were found to reduce to a compact set of Strouhal numbers ranging between $0.09 \leq St_\delta, St_{\delta,e} \leq 0.14$, as shown in Table 1. This range of displacement thickness-based Strouhal numbers is found to be consistent with the Strouhal number values reported in literature for a Kelvin-Helmholtz type instability of the separated shear layer across similar Reynolds numbers. This instability process had been conjectured previously, from the instantaneous Q-criterion contours presented in Fig. 16, as the driving mechanism behind the growth of small scale structures near the airfoil leading edge.

Table 1. Dominant frequency modes obtained from linear stability analysis at various Re_c.

Re_c ($\times 10^6$)	α (deg)	f (Hz)	f_e (Hz)	St_δ	$St_{\delta,e}$
0.20	18.64	210	230	0.13	0.14
0.50	20.63	300	275	0.10	0.09
1.00	24.72	370	260	0.14	0.10

Conclusions

The current study was conducted in order to characterize the quantitative spatiotemporal scales associated with the dynamic stall flow field across a transitional-Reynolds number regime. Across these higher Reynolds numbers, a series of flow field interactions were observed to produce a broad distribution of scales not observed in the canonical dynamic stall process at lower Reynolds numbers from the literature.

A series of high-frequency surface pressure measurements were used to identify the presence of a laminar separation bubble prior to the breakdown of the flow at the airfoil leading edge. The presence of this laminar separation bubble was observed to be associated with a characteristic frequency scale due to formation and shedding of vortex structures at a Strouhal number of $St_{LSB} = 1.2$, when the characteristic length scale was assumed to be the projected height of the laminar separation bubble. This characteristic frequency was not present when a boundary-layer trip was used to force transition prior to the separation bubble location, which reinforced the conclusion that the separation bubble was the source of this unsteadiness.

Off-body TR-PIV data were utilized to reveal the overall flow morphology associated with dynamic stall across transitional Reynolds numbers. Unlike the classical low-Reynolds number case, a series of lumped, coherent vortex structures were observed to dominate the instantaneous velocity field, which collectively produced the DSV. As the Reynolds number was increased from $Re_c = 0.2 \times 10^6$ and $Re_c = 0.5 \times 10^6$, to $Re_c = 1.0 \times 10^6$, the DSV was observed to be produced from a mutual roll-up of two bulk vortex flow structures, rather than forming from an initial vortex across the surface. These observations were consistent with similar conclusions from recent computational simulations.

In order to characterize the scales in the off-body velocity field, an EMD method was coupled to Hilbert spectral analysis to determine the time-dependent amplitudes and frequencies of each IMF. From this analysis it was shown that the breakdown of the flow at the airfoil leading edge results in a dramatic increase in amplitude of oscillations across very high frequencies. Further development of the DSV was observed to be associated with a broad series of scales, with the characteristic range of frequencies dependent on the Reynolds number. For the case of $Re_c = 1.0 \times 10^6$, a region of high-frequency content was observed in the velocity field near the surface, moving in the upstream direction prior to breakdown of the flow at the airfoil leading edge. These oscillations were produced by the upstream-moving region of turbulent separation from the trailing edge.

The EMD-Hilbert spectral analysis method was also compared to an analytical approach to predicting the spectral content of the off-body velocity oscillations through the use of a linear stability analysis. A numerical implementation of the Orr-Sommerfeld eigenvalue problem was used to determine the stability of the velocity field at select angles of attack, assuming a base flow from the phase-averaged velocity fields across multiple experimental interrogations. General agreement was observed with experimentally-derived values of the most unstable perturbation frequencies in the velocity field, with some slight disagreement at the higher Reynolds number ($Re_c = 1.0 \times 10^6$). However, both the analytical and experimental frequencies were observed to correspond to a range of Strouhal numbers, based on the shear-layer displacement thickness, of $0.09 \leq St_\delta$, $St_{\delta,e} \leq 0.14$. This range of Strouhal numbers is consistent with those associated with the Kelvin-Helmholtz instability for canonical subsonic shear layers. While the role of the Kelvin-Helmholtz instability in the formation of coherent vortex structures, significantly smaller than that of the DSV, has been conjectured in previous studies on dynamic stall. However, this quantitative analysis has confirmed this source of unsteadiness in the velocity field.

Personnel Supported

The current study supported work of the following personnel:

Faculty: Prof. Phillip Ansell (PI)
PhD Students: Rohit Gupta

Publications and Dissemination

Work performed during the current study was disseminated through the following publications and conference proceedings:

Gupta, R. and Ansell, P.J., "Unsteady Flow Physics of Airfoil Dynamic Stall," *AIAA Journal*, Vol. 57, No. 1, 2019, pp. 165-175. doi: 10.2514/1.J057257

Ansell, P.J. and Mulleners, K., "Multi-Scale Vortex Characteristics of Dynamic Stall from Empirical Mode Decomposition," *AIAA Journal* (Invited). doi: 10.2514/1.J057800

Gupta, R. and Ansell, P.J., "Unsteady Flow Physics of Airfoil Dynamic Stall," AIAA Paper 2017-0999, 2017.

Gupta, R. and Ansell, P.J., "Investigation of the Effects of Reynolds Number on the Unsteady Flow Physics of Airfoil Dynamic Stall," AIAA Paper 2018-0354, 2018.

Additionally, the following disseminations are anticipated over the year following this final report:

Gupta, R., "Unsteady Flow Physics of Airfoil Dynamic Stall," Ph.D. Dissertation, University of Illinois at Urbana-Champaign, 2019.

Presentation at 2019 APS-DFD conference

Two archival journal publications (in development)

Interactions/Transitions

a) The experiments conducted through this study have been of enduring interest to the Multidisciplinary Computational Aerodynamics Group at AFRL (Aerospace Systems Directorate). Discussions and data sharing between the current study and similar programs at AFRL have significantly aided the results of efforts across both institutions.
b) Results of this study have also permitted the expansion of international collaborative research through an AFOSR-sponsored International Student Exchange Program effort.
c) The EMD analysis of the off-body dynamic stall flow field has received enthusiastic interest from multiple research groups. This interest led to an invited talk, "Use of Empirical Mode Decomposition for Separation of Spatiotemporal Scales in Unsteady Flows," at the 2017 AIAA Aviation Forum. It has also gained the interest of the Army

Research Office, where a new study has been sponsored on the use of EMD to understand the nonlinear dynamics of natural boundary-layer transition.

New Discoveries, Inventions, or Patent Disclosures

None

Honors/Awards

Forbes Magazine, "30 Under 30" (Science Category), 2016
Army Research Office Young Investigator Award, 2017
University of Illinois, College of Engineering Dean's Award for Excellence in Research, 2019

References

[1] Granlund, K.O., Ol, M.V., Garmann, D.J., Visbal, M.R., and Bernal, L.P., "Experiments and Computations on Abstractions of Perching," AIAA Paper 2010-4943, 2010.

[2] Ol, M.V., Eldredge, J.F., and Wang, C., "High-Amplitude Pitch of a Flat Plate: an Abstraction of Perching and Flapping," *International Journal of Micro Air Vehicles*, Vol. 1, No. 3, 2009, pp. 203–216.

[3] McCroskey, W. J., "The Phenomenon of Dynamic Stall," NASA-TM-81264, 1981.

[4] Carr, L.W., "Progress in Analysis and Prediction of Dynamic Stall," *Journal of Aircraft*, Vol. 25, No. 1, 1988, pp. 6–17.

[5] Carr, L.W., McAlister, K.W., and McCroskey, W.J., "Analysis of the Development of Dynamic Stall based on Oscillating Airfoil Experiments," NASA-TN-D-8382, 1977.

[6] McAlister, K.W., Carr, L.W., and McCroskey, W.J., "Dynamic Stall Experiments on a NACA 0012 Airfoil," NASA-TP-1100, 1978.

[7] Visbal, M.R., "Dynamic Stall of a Constant-Rate Pitching Airfoil," *Journal of Aircraft*, Vol. 27, No. 5, 1990, pp. 400–407.

[8] Chandrasekhara, M.S., Carr, L.W., and Wilder, M.C., "Interferometric Investigations of Compressible Dynamic Stall over a Transiently Pitching Airfoil," *AIAA Journal*, Vol. 32, No. 3, 1994, pp. 586–593.

[9] Chandrasekhara, M.S., Ahmed, S., and Carr, L.W., "Schlieren Studies of Compressibility Effects on Dynamic Stall of Transiently Pitching Airfoils," *Journal of Aircraft*, Vol. 30, No. 2, 1993, pp. 213–220.

[10] Rival, D., and Tropea, C., "Characteristics of Pitching and Plunging Airfoils Under Dynamic-Stall Conditions," *AIAA Journal*, Vol. 47, No. 1, 2010, pp. 80–86.

[11] Pruski, B.J., and Bowersox, R.D.W., "Leading-Edge Flow Structure of a Dynamically Pitching NACA 0012 Airfoil," *AIAA Journal*, Vol. 51, No. 5, 2013, pp. 1042–1053.

[12] Mulleners, K., and Raffel, M., "The Onset of Dynamic Stall Revisited," *Experiments in Fluids*, Vol. 52, No. 3, 2012, pp. 779-793.

[13] Mulleners, K., and Raffel, M., "Dynamic Stall Development," *Experiments in Fluids*, Vol. 54, No. 2, 2013, pp. 1-9.

[14] Visbal, M.R., "Analysis of the Onset of Dynamic Stall Using High-Fidelity Large-Eddy Simulations," AIAA Paper 2014-0591.

[15] Lorber, P.F., and Carta, F.O., "Airfoil Dynamic Stall at Constant Pitch Rate and High Reynolds Number," AIAA Paper 87-1329.

[16] Barlow, J.B., Rae, W.H. Jr., and Pope, A., "Low-Speed Wind Tunnel Testing," 3rd Edition, *John Wiley & Sons, Inc*., New York, 1999.

[17] Torrence, C., and Compo, G.P., "A Practical Guide to Wavelet Analysis," *Bulletin of the American Meteorological Society,* Vol. 79, No. 1, 1998, pp. 61-78.

[18] Thirumalaisamy, M.R. and Ansell, P.J., "Fast and Adaptive Empirical Mode Decomposition for Multidimensional, Multivariate Signals," *IEEE Signal Processing Letters*, Vol. 25, No. 10, 2018, pp. 1550-1554. doi: 10.1109/LSP.2018.2867335

[19] Benton, S.I. and Visbal, M.R., "Understanding Abrupt Leading Edge Separation as a Mechanism for the Onset of Dynamic Stall," AIAA Paper 2018-0356, 2018.